Benchtop characterization of the tricuspid valve leaflet pre-strains

Devin W. Laurence[a], Colton J. Ross[a], Ming-Chen Hsu[b], Arshid Mir[c], Harold M. Burkhart[d], Gerhard A. Holzapfel[e,f], Chung-Hao Lee[a,*]

[a]*Biomechanics & Biomaterials Design Lab, School of Aerospace & Mechanical Eng., University of Oklahoma, USA*
[b]*Computational Fluid-Structure Interaction Laboratory, Department of Mechanical Eng., Iowa State University, USA*
[c]*Department of Pediatrics, University of Oklahoma Health Sciences Center, USA*
[d]*Department of Surgery, University of Oklahoma Health Sciences Center, USA*
[e]*Institute of Biomechanics, Graz University of Technology, Austria*
[f]*Department of Structural Engineering, Norwegian University of Science and Technology, Norway*

Abstract

The pre-strains of biological soft tissues are important when relating their *in vitro* and *in vivo* mechanical behaviors. In this study, we present the *first-of-its-kind* experimental characterization of the tricuspid valve leaflet pre-strains. We use 3D photogrammetry and the reproducing kernel method to calculate the pre-strains within the central 10×10 mm region of the tricuspid valve leaflets from $n = 8$ porcine hearts. In agreement with previous pre-strain studies for heart valve leaflets, our results show that all the three tricuspid valve leaflets shrink after explant from the *ex vivo* heart. These calculated strains are leaflet-specific and the septal leaflet experiences the most compressive changes. Furthermore, the strains observed after dissection of the central 10×10 mm region of the leaflet are smaller than when the valve is explanted, suggesting that our computed pre-strains are mainly due to the release of *in situ* annulus and chordae connections. The leaflets are then mounted on a biaxial testing device and preconditioned using force-controlled equibiaxial loading. We show that the employed preconditioning protocol does not 100% restore the leaflet pre-strains as removed during tissue dissection, and future studies are warranted to explore alternative preconditioning methods. Finally, we compare the calculated biomechanically oriented metrics considering five stress-free reference configurations. Interestingly, the radial tissue stretches and material anisotropies are significantly smaller compared to the post-preconditioning configuration. Extensions of this work can further explore the role of this unique leaflet-specific leaflet pre-strains on *in vivo* valve behavior via high-fidelity *in-silico* models.

Keywords: configurational changes, valve tissue biomechanics, preconditioning, direct linear transformation, reproducing kernel method, 3D photogrammetry

1. Introduction

All biological soft tissues are naturally strained in their *in vivo* configuration. Chuong and Fung [1] discovered these pre-strains in their seminal experimental investigation of arterial opening angles. Despite their conceptual simplicity, pre-strains have profound implications for soft tissue biomechanics and how we interpret the mechanical behavior of tissues *in vivo*. For example, *in vitro* mechanical characterizations use a stress-free reference configuration that does not take into account the tissue pre-strains. Due to the lack of consideration of the pre-strains, the subsequent *in-silico* simulations, which are based on the obtained *in vitro* experimental data, would lead to very different predictions

*Corresponding author. 865 Asp Ave., Felgar Hall 219C, Norman, OK 73019, USA.
Email address: ch.lee@ou.edu (Chung-Hao Lee)

of the *in vivo* tissue behavior. This dilemma leads us to a long-standing question in the soft tissue biomechanics community: *How can we relate the in vitro and in vivo configurations to provide reliable in-silico predictions of soft tissue bio-systems?*

The tricuspid valve has received increased attention since Dreyfus *et al.* [2] and Anyanwu and Adams [3] established its clinical relevance and more appropriate surgical considerations. Basic science approaches to understanding the tissue biomechanics of the tricuspid valve can be divided into *in vitro* characterizations, *ex vivo* or *in vivo* investigations and *in-silico* predictions (see also the extensive reviews in [4, 5]). For *in vitro* characterizations, researchers have used biaxial tests [6, 7] to characterize the mechanical properties of the leaflets. Interestingly, it was shown that the mechanical properties are leaflet-specific [8–10], spatially heterogeneous [11], and transmurally different [12]. Recent efforts have further advanced our understanding by linking these mechanical behaviors to the underlying collagen fiber architecture and layered microstructure [10, 13, 14]. In contrast to *in vitro* characterizations, *ex vivo* and *in vivo* studies attempt to understand the leaflet behavior within the native functional environment (i.e., realistic hemodynamics and *in situ* connections). These investigations have confirmed the *in vitro* findings that the quantified properties are leaflet-specific and spatially heterogeneous [15, 16]. A major advantage of *ex vivo* and *in vivo* models is that the leaflet behavior and properties are determined with the inherent pre-strains taken into account. Finally, *in-silico* investigations attempt to utilize data from *in vitro*, *ex vivo*, and *in vivo* studies to predict the *in vivo* valve function. The tricuspid valve geometry for these studies is traditionally derived from segmented medical imaging data [17, 18] or measurements of explanted leaflet dimensions in conjunction with the natural cubic splines [19] or non-uniform rational basis splines (NURBS) [20, 21]. For simulations using segmented valve geometry, researchers can utilize inverse modeling [22] to ensure that the predictions are consistent with medical imaging data by estimating the *in vivo* material parameters for the valve leaflets. This may lead to accurate simulation predictions of valve function, but inaccurate leaflet mechanical behavior since the pre-strains are implicitly embedded within the simulation. On the other hand, simulations using the explanted leaflet measurements can use the exact mechanical behaviors determined from *in vitro* experiments. However, as mentioned above, these do not take tissue pre-strains into account and lead to incorrect predictions of the biomechanical behavior of the valve.

In the soft tissue biomechanics literature, the pre-strains of various biological tissues have been examined using three general approaches: (i) opening angle experiments, (ii) tissue excision and incision experiments, and (iii) *in-silico* numerical investigations. For opening angle experiments, thin rings of tissue are floated on a liquid bath and cut to release the pre-strains. The ring of tissue then opens at a certain angle that indicates the amount of pre-strain present in the tissue. Recent studies have expanded on this original technique by Y.C. Fung [1, 23, 24] to provide a refined pre-strain field of the annulus fibrosis [25], the arteries [26–28], the left ventricle [29], and the epicardium [30]. This method is versatile and can be easy to implemented for new tissues; however, it is only valid for ring-like tissues and may not be directly applicable to other planar tissues such as the heart valve leaflets. With these planar tissues, researchers typically resort to excising or incising the tissues and monitoring the associated configurational changes (i.e., release of pre-strains). This was done for the mitral valve [31, 32], the aortic valve [33–35], the skin [36–38], and the tympanic membrane [39]. For the third category, researchers develop *in-silico* models to explore the role of pre-strain in the leaflet behavior. Previous work has focused on virtual configurations for embedding the residual strains in elastic materials, which form the basis for these developments [40, 41]. Although the pre-strains are not experimentally quantified, this method leads to a range of possible pre-strains that can be used for later simulations. The developed platforms can also facilitate numerical investigations of the pre-strains to understand the associated etiology. Rausch and Kuhl [42] pioneered this approach for the mitral valve and discovered that including pre-strains in the model can change the predicted tissue stiffness by three orders of magnitude. *In-silico* methods were later used to estimate the pre-strains of

the mitral valve leaflets [43] whether cell-mediated forces could produce a reasonable range of pre-strains [44], the mitral valve chordae tendineae [45] and recently the effect of viscoelasticity on the residual stresses of arteries [46].

Despite tremendous advances in tricuspid valve biomechanics, there is a significant gap in connecting our *in vitro*, *ex vivo*, and/or *in vivo* experimental results to *in-silico* model developments. The aim of this study is therefore to characterize the *ex vivo* tricuspid valve leaflet pre-strains, taking inspiration from previous studies performed for the mitral valve leaflets (e.g., [31]) and the skin (e.g., [36, 37]). We accomplish this by using a novel approach that combines 3D photogrammetry and the reproducing kernel method [47, 48] to quantify the tricuspid valve leaflet strains after dissection from the heart. Briefly, 3D photogrammetry is used to determine the 3D locations of a 3×3 grid of fiducial markers associated with three important *in vitro* experimental configurations: the *ex vivo* heart, the explanted valve and the dissected specimen. The specimens are then mounted on the biaxial tester for force-controlled preconditioning to observe how the typical *in vitro* stress-free reference configuration compares to the *ex vivo* configurations. We further explore how the choice of the reference configuration affects key biomechanics metrics at peak equibiaxial membrane tensions. Finally, we evaluate our results in the context of previous findings for the other heart valve leaflets and other porcine tissues.

2. Materials and Methods

2.1. Heart Acquisition and Preparation

Eight adult porcine hearts ($n = 8$, 80-140 kg, 1-1.5 years of age) were transported from a local USDA-approved abattoir (Chickasha Meat Company, Chickasha, OK) to our laboratory. The auricles were removed, and the right ventricle was opened by cutting along the posterior-septal commissure to the apex of the heart. The central 10×10 mm testing region of each tricuspid valve leaflet was delimited by four surgical pen dots, and 9 glass beads (arranged in a 3×3 grid) were affixed within this region using cyanoacrylate glue (Fig. 1(a)).

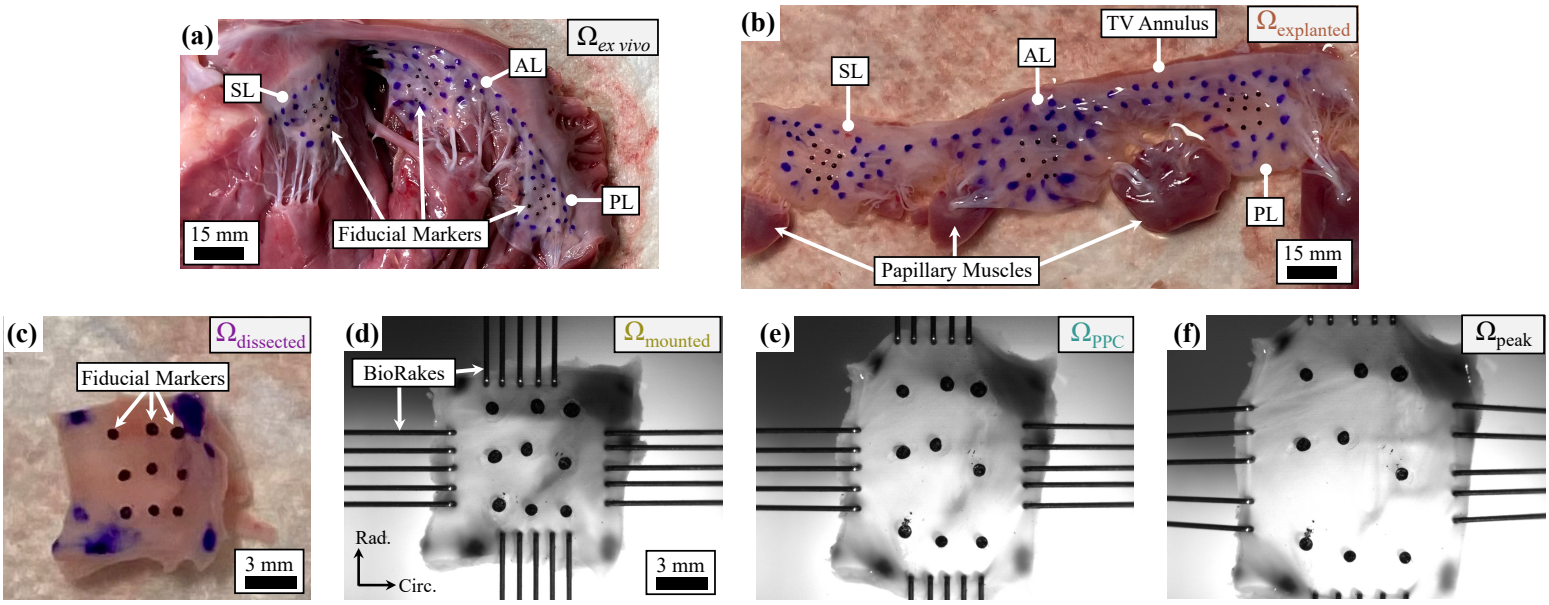

Figure 1: Representative experimental images of: (a) the opened right ventricle with fiducial markers affixed to the central region of each tricuspid valve leaflets ($\Omega_{ex\,vivo}$), (b) the explanted tricuspid valve while maintaining valvular connections ($\Omega_{\text{explanted}}$), (c) the dissected 10×10 mm anterior leaflet specimen ($\Omega_{\text{dissected}}$), (d) the specimen mounted to the CellScale BioTester (Ω_{mounted}), (e) the post-preconditioned specimen (Ω_{PPC}), and (f) the specimen at peak equibiaxial tensions of 40 N/m (Ω_{peak}). Abbreviations: AL = anterior leaflet, PL = posterior leaflet, SL = septal leaflet, Circ = circumferential direction, Rad = radial direction.

2.2. Reconstruction of Marker 3D Coordinates and Dissection of the Tricuspid Valve

Two cameras arranged in a stereo configuration were used to capture images of the tricuspid valve in three configurations (Fig. 1(a)-(c)): (i) the *ex vivo* configuration ($\Omega_{ex\,vivo}$), (ii) the explanted configuration ($\Omega_{\text{explanted}}$), and (iii) the dissected specimen configuration ($\Omega_{\text{dissected}}$). The opened right ventricle was first placed beneath the cameras to capture images of the *ex vivo* configuration (Fig. 1(a)). Next, the tricuspid valve, including the annulus and the chordal connections to the papillary muscles, was dissected and floated on a shallow bath of phosphate buffered saline (PBS) to image the *explanted* configuration (Fig. 1(b)). Finally, the central 10×10 mm region of each leaflet (i.e., tricuspid valve anterior leaflet, posterior leaflet, and septal leaflet) was excised and floated on the PBS bath to image the *dissected* specimen configuration (Fig. 1(c)).

The two images acquired by dual cameras for each of the above three tricuspid valve configurations were imported into MATLAB (MathWorks, Natick, MA). The pixel locations (p_i,q_i) of the nine fiducial markers ($i = 1, \ldots, 9$) captured by the two cameras were obtained using the `drawpolygon()` function in MATLAB. The pixel locations were combined with the calibrated direct linear transformation (see more details in Appendix A) to determine the 3D locations of the fiducial markers (Fig. 2(a)) [49].

2.3. Preconditioning Step of Planar Biaxial Mechanical Testing

Then, the 10×10 mm specimen was mounted on a commercial biaxial mechanical testing system (BioTester, CellScale, Ontario, Canada) with an effective testing region of 7×7 mm (Fig. 1(d)). Starting from this *mounted* configuration (Ω_{mounted}), the specimens were pre-tensioned and then subjected to 10 cycles of force-controlled preconditioning to achieve peak equibiaxial membrane tensions of 40 N/m [8] (i.e., 280 mN). For this study, the applied pre-tension was 2.5% of the peak membrane tension (i.e., 7 mN) [11, 12], the loading was applied at an approximately quasi-static loading rate ($2 - 3$%/s), and the tissue was maintained at 32 °C due to the lens fogging limitation of our integrated opto-mechanical device [14, 50]. During the test, 1280×960 resolution images of the fiducial markers were captured by a CCD camera and load cell values were recorded at 10 Hz throughout testing. The *post-preconditioned* (PPC) configuration (Ω_{PPC}) [9] was assumed as the stress-free configuration after the tenth force-controlled loading cycle. In addition, the configuration associated with the peak biaxial tensions of the tenth loading cycle (Ω_{peak}) was used to analyzed tissue stretches with respect to each of the five configurations shown in Fig. 1.

2.4. Calculation of the Tricuspid Valve Leaflet Pre-Strains

The reproducing kernel (RK) method [47, 48] (Appendix B) was used to determine the deformation gradient $\mathbf{F}$ from the *ex vivo* configuration to the explanted, dissected, mounted, post-preconditioned, and peak-tension configurations. The partial derivatives of the RK shape functions Ψ_I were combined with the fiducial marker displacements $[\mathbf{d}_I(t)] = [u_I(t), v_I(t), w_I(t)]^{\mathrm{T}}$ (Fig. 2(c)-(d)) to compute the deformation gradient, i.e.,

$$[\mathbf{F}] = [\mathbf{F}(\mathbf{X}, t)] = [\mathbf{I}] + \begin{bmatrix} \sum_{I=1}^{NP} \Psi_{I,x} u_I(t) & \sum_{I=1}^{NP} \Psi_{I,y} u_I(t) & \sum_{I=1}^{NP} \Psi_{I,z} u_I(t) \\ \sum_{I=1}^{NP} \Psi_{I,x} v_I(t) & \sum_{I=1}^{NP} \Psi_{I,y} v_I(t) & \sum_{I=1}^{NP} \Psi_{I,z} v_I(t) \\ \sum_{I=1}^{NP} \Psi_{I,x} w_I(t) & \sum_{I=1}^{NP} \Psi_{I,y} w_I(t) & \sum_{I=1}^{NP} \Psi_{I,z} w_I(t) \end{bmatrix}. \tag{1}$$

The deformation gradient $\mathbf{F}$ at each of the chosen nine isoparametric locations (Fig. 2(b)) was further transformed into the Green-Lagrange strain $\mathbf{E} = \frac{1}{2}(\mathbf{F}^{\mathrm{T}}\mathbf{F} - \mathbf{I})$ [51]. The principal values and principal directions of $\mathbf{E}$ were next used to determine the *in-plane* principal strains and areal strains of the tricuspid valve leaflets. Due to experimental limitations in quantifying the change in the tissue thickness direction between different configurations, we did not consider or examine the tissue incompressibility that is a common assumption adopted in the heart valve biomechanics literature [52, 53]. Therefore, the principal value aligned with the tissue's transmural direction (determined via its principal direction)

was disregarded in our overall pre-strain analyses. The remaining in-plane principal values were categorized as the maximum principal strain E_1, and the minimum principal strain E_2, which were used to compute the maximum shear strain $\gamma = \frac{1}{2}(E_1 - E_2)$. Finally, the associated principal stretches λ_1 and λ_2 were used to compute the areal stretch $\lambda_A = \lambda_1\lambda_2$, and, subsequently, the areal strain $E_A = \frac{1}{2}({\lambda_A}^2 - 1)$.

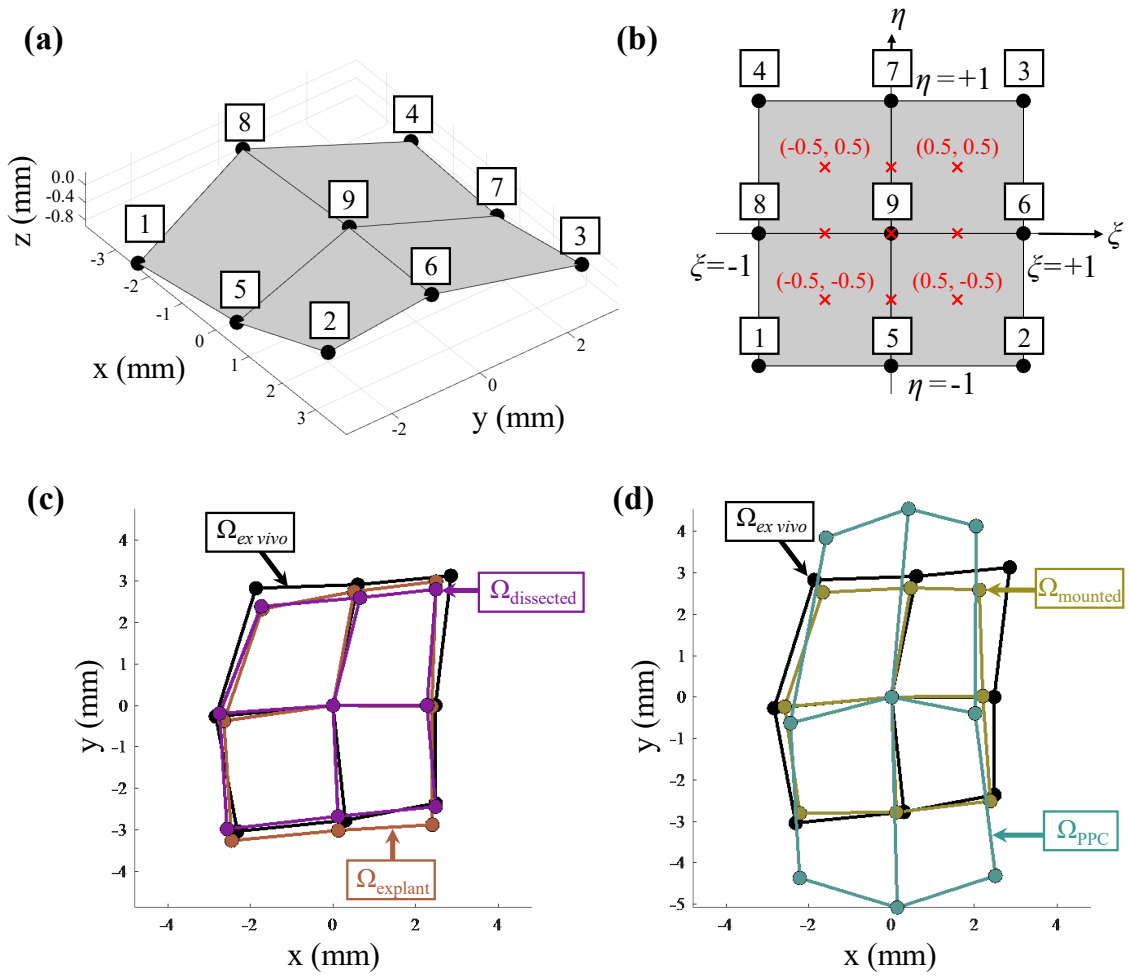

Figure 2: (a) Reconstructed 3D locations of the fiducial marker grid using calibrated direct linear transformation-based photogrammetry (see Appendix A). (b) Nine isoparametric locations (red crosses) chosen to assess tricuspid valve leaflet pre-strains for regional analysis. (c),(d) Results of the tricuspid valve leaflets of a representative porcine heart: fiducial marker locations for calculating the deformation gradient for *Analysis I* and *Analysis II*, respectively. Note that the fiducial marker locations shown in (c),(d) are in the 3D space and only the x- and y-components are shown as a 2D projection for visualization purposes.

2.5. Data Analysis

Analysis I: Ex Vivo Pre-Strains. The primary objective of this study was to quantify the *ex vivo* pre-strains for all three tricuspid valve leaflets. Therefore, our first analysis aimed to compare the in-plane principal strains and the areal pre-strain between the explanted and dissected configurations at the center of the specimen, i.e., $(\xi, \eta) = (0, 0)$ (Fig. 2(b)). Since our preliminary qualitative assessment revealed that the pre-strains were spatially heterogeneous, we also compared the areal pre-strains between the nine isoparametric locations defined in Fig. 2(b).

Analysis II: Biaxial Testing Configurations. Besides quantifying the *ex vivo* tricuspid valve leaflet pre-strains, we were also interested in understanding how the mounted and PPC configurations relate

to the *ex vivo* configurations. The stress-free reference configuration is an important consideration for mechanical characterizations [1, 9, 10, 31, 42], so it is crucial to understand how these two common reference configurations in the benchtop tissue characterization procedures compare to the more realistic *ex vivo* configuration. Therefore, our second analysis focused on comparing the principal and areal pre-strains for the mounted and PPC configurations. Similar to the analysis of the *ex vivo* pre-strains in *Analysis I*, we compared these values between the nine isoparametric locations as shown in Fig. 2(b).

Analysis III: Stress-Free Reference Configurations. Our final analysis was an extension of *Analysis II* but focused more on understanding the role of *ex vivo* pre-strains play in the characterized mechanical behaviors of tissues. To facilitate this comparison, we computed several common biomechanics-based metrics derived from the biaxial mechanical characterizations for the five reference configurations. This included the peak stretches in the circumferential (λ_{circ}) and radial (λ_{rad}) tissue directions and the anisotropy index $AI = \lambda_{rad}/\lambda_{circ}$ [9, 10].

2.6. Statistical Analysis

Data are presented as mean ± standard error of the mean (SEM). Quantile-quantile (Q-Q) plots (not shown here) revealed that the data was not normally distributed in general. Thus, two-factor comparisons (configuration vs. leaflet) of the principal pre-strains (E_1, E_2), the areal pre-strain (E_A), the computed leaflet stretches (λ_{circ},λ_{rad}), and the anisotropy index (AI) were made using the non-parametric aligned rank transform [54]. Further contrast tests were performed using the aligned rank transform contrasts method [55]. The non-parametric Kruskal-Wallis test was also employed to determine statistically significant differences in the computed pre-strains among the nine isoparametric locations. Differences were considered as statistically significant when $p < 0.05$.

3. Results

The quantified areal pre-strains of one representative porcine heart for the explanted ($\Omega_{explanted}$), dissected ($\Omega_{dissected}$), mounted ($\Omega_{mounted}$), and PPC (Ω_{PPC}) configurations are shown in Fig. 3. These color maps highlight the leaflet-specific and heterogeneous nature of the quantified pre-strains. Further analyses of these results considering all the $n = 8$ porcine hearts are provided in the following subsections.

3.1. TV Leaflet Pre-Strains After Valve Dissection and Biaxial Testing Specimen Excision

The pre-strains presented in Fig. 4 show minimal differences between the explanted and dissected configurations, while Table 1 shows no significant differences between these two configurations. Throughout these comparisons, there was a consistent trend of the septal leaflet exhibiting more compressive pre-strains compared to the anterior leaflet. This difference was significant for the maximum principal pre-strain ($E_1 = -0.071 \pm 0.044$ vs. 0.130 ± 0.068) and the areal pre-strain ($E_A = -0.244 \pm 0.039$ vs. 0.018 ± 0.082) in the dissected configuration, as well as the areal pre-strain ($E_A = -0.252 \pm 0.041$ vs. -0.033 ± 0.060) in the explanted configuration with respect to $\Omega_{ex\ vivo}$. There were also significant differences when comparing the maximum principal pre-strains of the septal leaflet in the explanted configuration (-0.070 ± 0.042) to the anterior leaflet in the dissected configuration (0.130 ± 0.068), and when comparing the areal strains of both leaflets in the explanted (septal: -0.252 ± 0.041, anterior: -0.033 ± 0.060) and dissected (septal: -0.244 ± 0.039, anterior: -0.018 ± 0.082) configurations. No significant differences were found when comparing the posterior leaflet to the septal leaflet or anterior leaflet.

3.2. *Comparison of the Mounted and PPC Configurations with the Ex Vivo Configuration*

The comparisons of pre-strains in Fig. 5 and Table 1 reveal significant differences between the mounted and PPC configurations. Interestingly, no significant differences were found between the three leaflets within one configuration. For the minimum principal pre-strain, the mounted septal leaflet (-0.186 ± 0.023) was significantly lower than the post-preconditioned anterior (0.049 ± 0.070), posterior (0.002 ± 0.052), and septal (-0.027 ± 0.046) leaflets. On the other hand, the maximum principal pre-strains for the anterior (0.150 ± 0.067), posterior (0.049 ± 0.033), and septal (-0.015 ± 0.039) leaflets were significantly smaller in the mounted configuration than for the anterior (0.751 ± 0.096) and posterior (0.754 ± 0.064) leaflets in the PPC configuration. Only the septal leaflet's maximum principal pre-strain (-0.015 ± 0.039) in the mounted configuration was smaller than that for the septal leaflet (0.419 ± 0.138) in the PPC configuration. With respect to the areal pre-strain, all but the mounted anterior leaflet (0.053 ± 0.092) and the post-preconditioned septal leaflet (0.318 ± 0.076) were statistically different. Finally, significant differences in maximum shear strain were found between the mounted septal leaflet (0.086 ± 0.019) and the post-preconditioned anterior (0.351 ± 0.055) and posterior leaflets (0.376 ± 0.038), as well as the mounted anterior leaflet (0.118 ± 0.032) and the post-preconditioned posterior leaflet (0.376 ± 0.038).

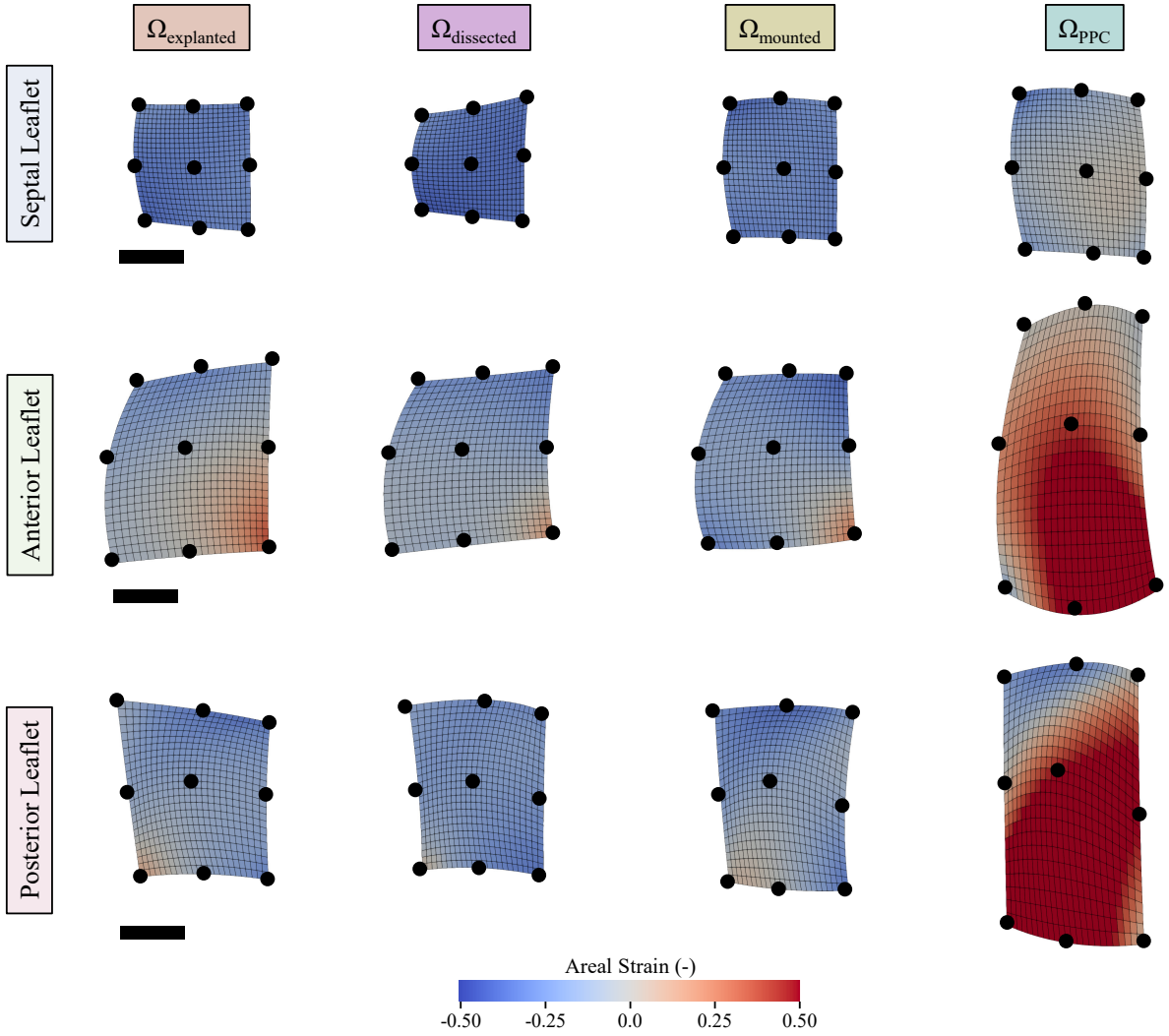

Figure 3: Results of the tricuspid valve leaflets of a representative porcine heart: visualization of the areal pre-strains E_A calculated in relation to the explanted configuration $\Omega_{explanted}$, dissected configuration $\Omega_{dissected}$, mounted configuration $\Omega_{mounted}$, and post-preconditioned (PPC) configuration Ω_{PPC}. Scale bars = 2 mm.

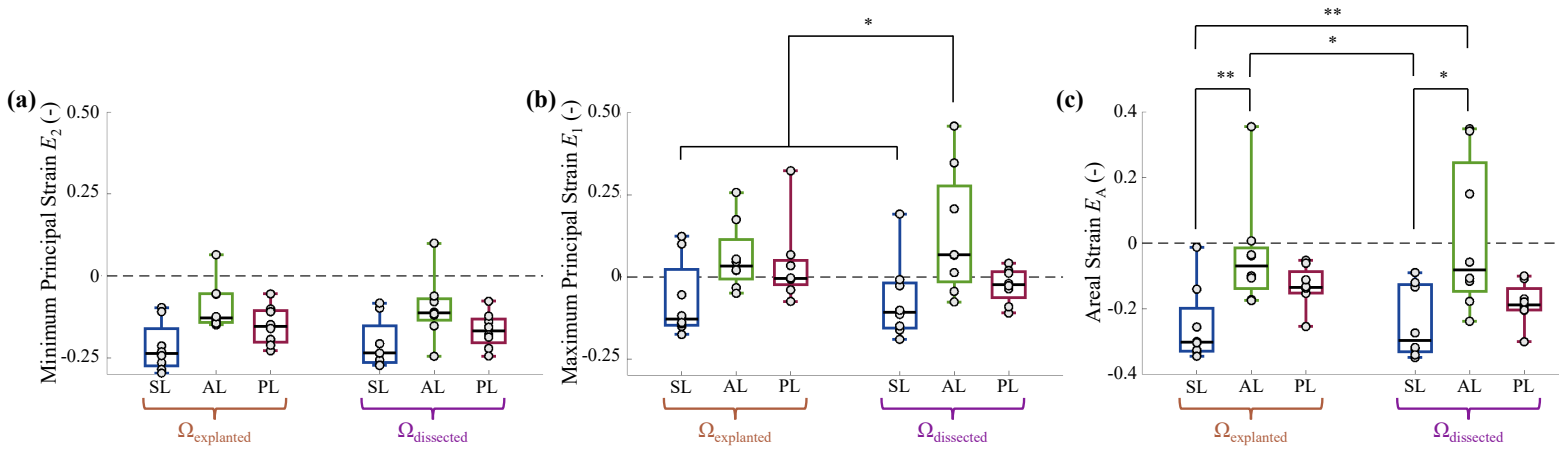

Figure 4: Computed pre-strains of the explanted configuration ($\Omega_{\text{explanted}}$) and the dissected configuration ($\Omega_{\text{dissected}}$) with respect to the *ex vivo* configuration ($\Omega_{ex\,vivo}$): (a) the minimum principal strain (E_2), (b) the maximum principal strain (E_1), and (c) the areal strain (E_A). Significance level: $*$ denotes $p < 0.05$, $**$ denotes $p < 0.01$. Abbreviations: AL = anterior leaflet, PL = posterior leaflet, SL = septal leaflet.

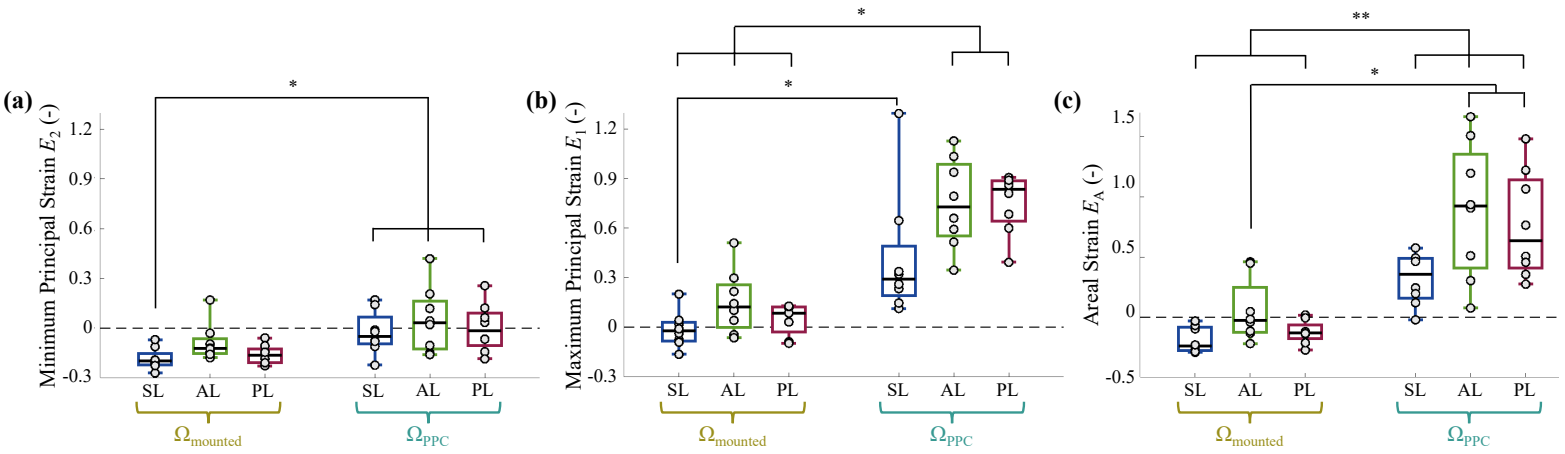

Figure 5: Computed pre-strains of the mounted configuration (Ω_{mounted}) and the PPC configuration (Ω_{PPC}) with respect to the *ex vivo* configuration ($\Omega_{ex\,vivo}$): (a) the minimum principal strain (E_2), (b) the maximum principal strain (E_1), and (c) the areal strain (E_A). Significance level: $*$ denotes $p < 0.05$, $**$ denotes $p < 0.01$. Abbreviations: AL = anterior leaflet, PL = posterior leaflet, SL = septal leaflet.

Table 1: Maximum shear strain of the three tricuspid valve leaflets computed with respect to $\Omega_{ex\,vivo}$.

Tricuspid Valve Leaflet	Configuration			
	$\Omega_{\text{Explanted}}$	$\Omega_{\text{Dissected}}$	Ω_{Mounted}	Ω_{PPC}
Septal Leaflet (SL)	0.074 ± 0.021	0.069 ± 0.022	0.086 ± 0.019	0.223 ± 0.084
Anterior Leaflet (AL)	0.076 ± 0.014	0.114 ± 0.032	0.118 ± 0.032	0.351 ± 0.055
Posterior Leaflet (PL)	0.094 ± 0.029	0.070 ± 0.012	0.105 ± 0.018	0.376 ± 0.038

3.3. TV Leaflet Biaxial Mechanical Properties Considering Different Reference Configurations

The biaxial testing parameters derived with respect to the five reference configurations are presented in Fig. 6. In the circumferential direction of the tissue, the only significant differences were found for the septal leaflet, where the stretches λ_{circ} with reference to $\Omega_{\text{dissected}}$ (1.486 ± 0.079) and Ω_{mounted} (1.467 ± 0.075) were significantly larger than those calculated at $\Omega_{ex\,vivo}$ (1.179 ± 0.058) and Ω_{PPC} (1.169 ± 0.020). On the other hand, the radial stretches λ_{rad} for the anterior and posterior leaflets

determined with respect to Ω_{PPC} (anterior: 1.140 ± 0.022, posterior: 1.127 ± 0.016) were found to be significantly smaller than the radial stretches considering the other four configurations (anterior: 1.617-1.741, posterior: 1.741-1.901). The septal leaflet radial stretches from Ω_{PPC} (1.167±0.032) were only significantly smaller than the stretches determined using $\Omega_{explanted}$ (1.820 ± 0.120) and $\Omega_{dissected}$ (1.710 ± 0.090). Eventually, the anisotropy ratio became approximately 1.0 for all the three leaflets. This change was significant for the anterior and posterior leaflets but was not found to be significant for the septal leaflet. In particular, the *AI* for the anterior leaflet was significantly smaller from Ω_{PPC} (0.972 ± 0.032) than $\Omega_{ex\ vivo}$ (1.396 ± 0.102) and $\Omega_{explanted}$ (1.351 ± 0.080). However, the posterior leaflet anisotropy (0.939 ± 0.006) was significantly different when using Ω_{PPC} than in all four other configurations (1.238-1.501).

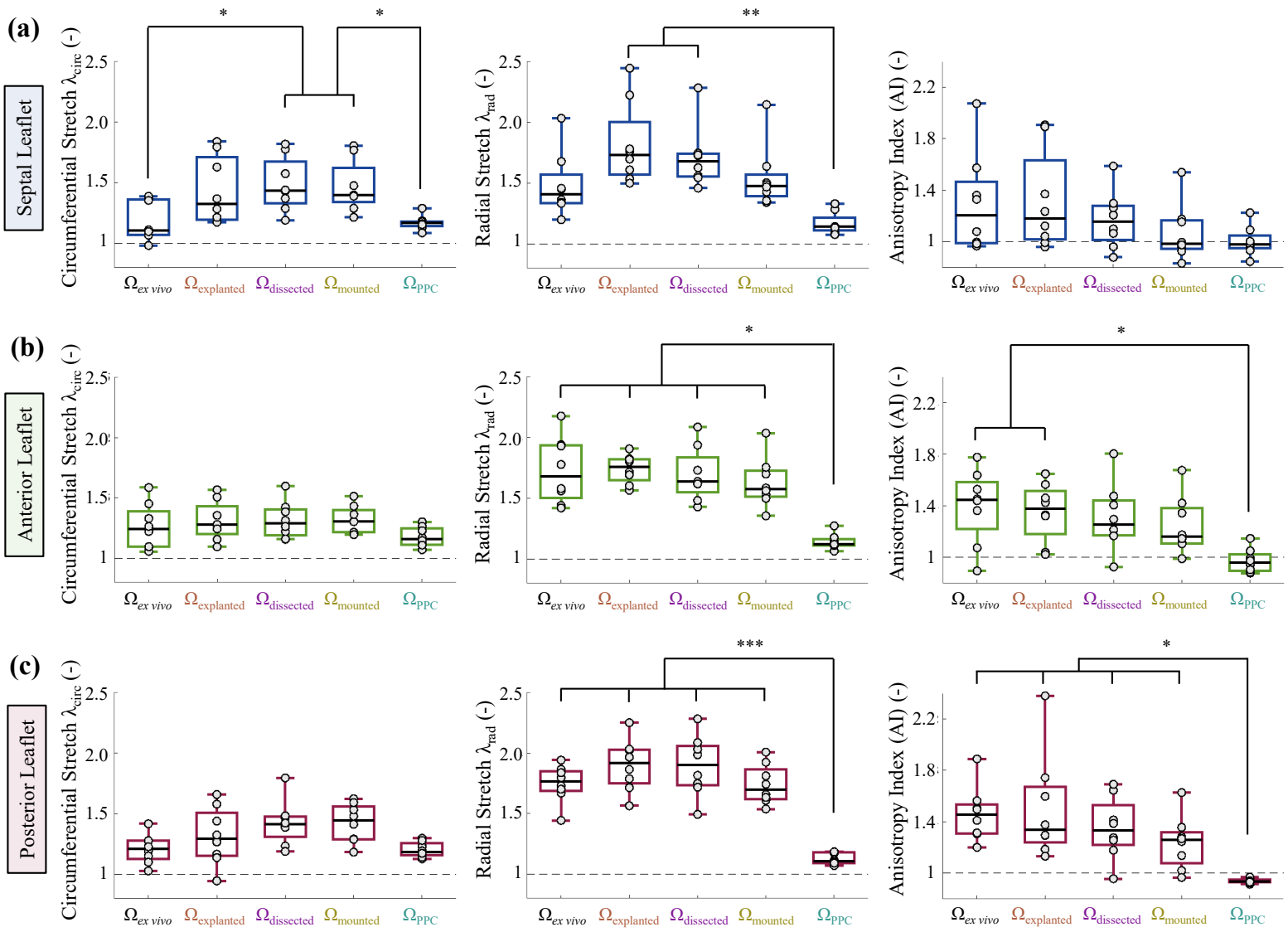

Figure 6: (*left*) circumferential stretch λ_{circ}, (*middle*) radial stretch λ_{rad}, and (*right*) anisotropy index (*AI*) calculated with respect to the five reference configurations for: (a) the septal leaflet, (b) the anterior leaflet, and (c) the posterior leaflet. (Significance levels: $*$ denotes $p < 0.05$, $**$ denotes $p < 0.01$, $***$ denotes $p < 0.001$.)

3.4. Regional Variations in TV Leaflet Areal Pre-Strains

The areal pre-strains E_A of the tricuspid valve leaflets at the nine isoparametric locations (Fig. 2(b)) are shown in Figs. 7 and 8 for the four configurations with reference to $\Omega_{ex\ vivo}$. These results reveal rel-

atively large variations in the pre-strains compared to the results in Figs. 4 and 5 for the central location, i.e., $(\xi, \eta) = (0, 0)$ in Fig. 2(b). Despite these regional variations, no statistically significant differences were found for the explanted areal pre-strains (septal: +0.021, anterior: −0.093, posterior: +0.020), the dissected areal pre-strains (septal: +0.019, anterior: −0.138, posterior: +0.043), the mounted areal pre-strains (septal: +0.061, anterior: −0.191, posterior: 0.065), and the post-preconditioned areal pre-strains (septal: −0.129, anterior: −0.503, posterior: −0.279).

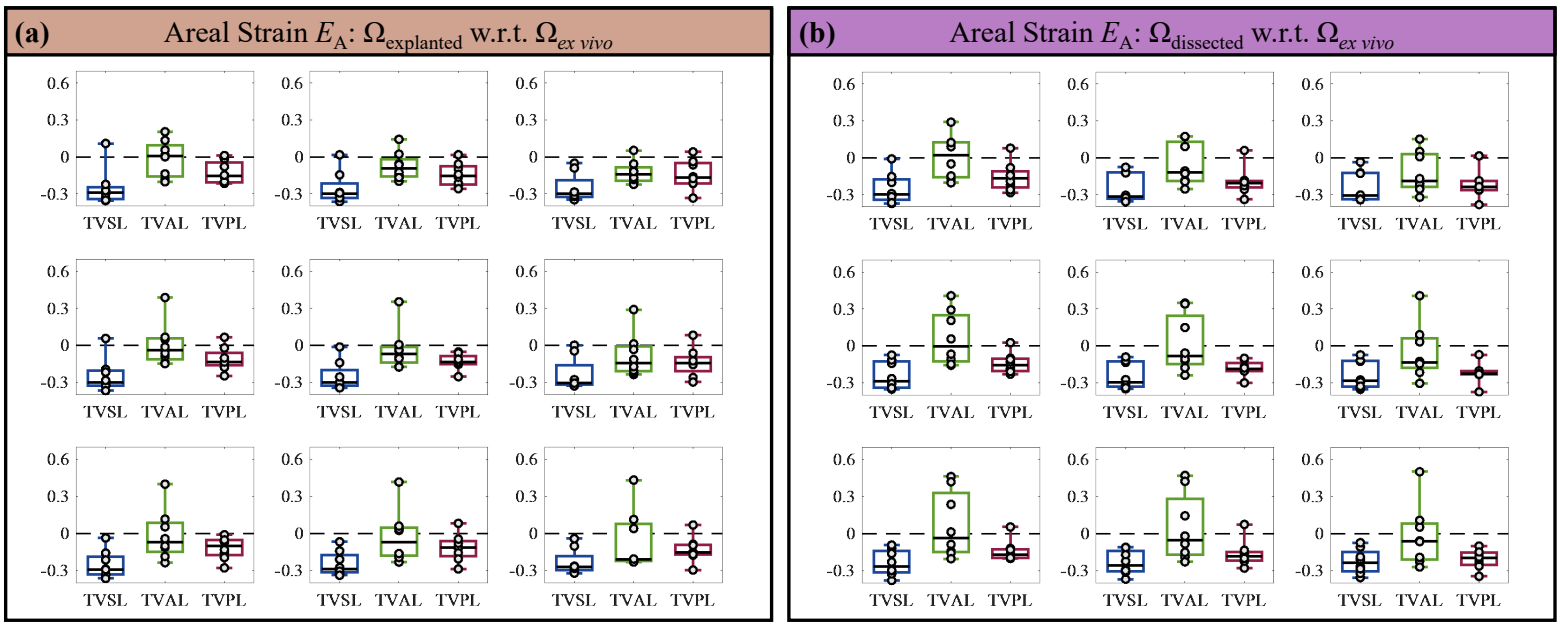

Figure 7: Areal pre-strains (E_A) calculated at the nine isoparametric locations (see Fig. 2(b)) for: (a) the explanted configuration ($\Omega_{explanted}$), and (b) the dissected configuration ($\Omega_{dissected}$), with respect to the *ex vivo* configuration ($\Omega_{ex\ vivo}$). Abbreviations: TV = tricuspid valve, AL = anterior leaflet, PL = posterior leaflet, SL = septal leaflet.

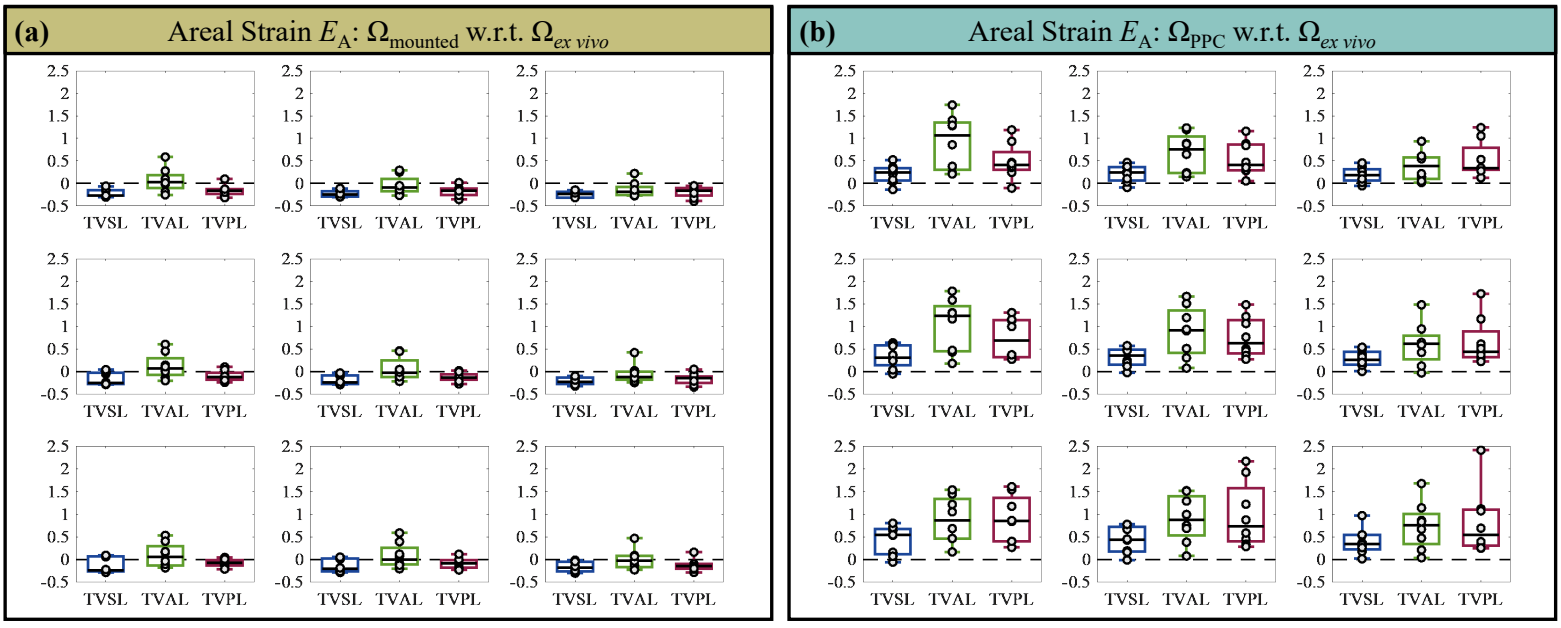

Figure 8: Areal pre-strains calculated at the nine isoparametric locations (see Fig. 2(b)) for: (a) the mounted configuration ($\Omega_{mounted}$), and (b) the PPC configuration (Ω_{PPC}), with respect to the *ex vivo* configuration ($\Omega_{ex\ vivo}$). Abbreviations: TV = tricuspid valve, AL = anterior leaflet, PL = posterior leaflet, SL = septal leaflet.

4. Discussion

4.1. Overall Findings

For the first time we have characterized the *ex vivo* pre-strains for the *tricuspid valve leaflets*. In the present work, we combined 3D photogrammetry with the reproducing kernel method to calculate the leaflet pre-strains at four key configurations associated with the usual tissue preparation procedures in the *in vitro* mechanical characterization experiments. This integrated approach allowed us to understand the kinematic changes of the central 10×10 mm region for each of the three tricuspid valve leaflets as it was gradually released from its *ex vivo* configuration and mounted on the biaxial testing device. We further explored how these reference configurations influenced the biaxial mechanical behaviors of the tricuspid valve leaflets. In particular, we gained new insights into how the stress-free reference configuration affects the leaflet mechanical properties typically reported in the literature (i.e., λ_{circ}, λ_{rad}, AI).

4.1.1. The Tricuspid Valve Leaflet Pre-Strains

Overall, we found that the three tricuspid valve leaflets shrunk after excision from the heart. This compressive deformation was smaller in magnitude for the anterior leaflet ($E_A = -0.033$) when compared to the septal ($E_A = -0.252$) and posterior leaflets ($E_A = -0.132$). Our previous biaxial mechanical characterization of porcine tricuspid valve leaflets [9] showed a similar trend, with the anterior leaflet being the stiffest of the three tricuspid valve leaflets. Interestingly, there were much smaller strains after dissection of the central 10×10 mm specimen (E_A = 1-5%) than after explantation of the valve from the heart. This indicates that most of the pre-strains observed in our experimental setup were due to the release of the annulus and chordae tendineae from their *in situ* connections to the heart chambers.

When the specimens were mounted on the biaxial testing device, we found that they were subjected to slight tensile strains due to their dissected configurations (E_A = +5-6%). However, this accidental tensile strain during mounting was not enough to restore the *ex vivo* leaflet configuration, and all three leaflets were still mostly under large compressive strains ($E_A = -5\%$ to -19%). that This is consistent with previous suggestions viscoelastic soft tissues must undergo some form of preconditioning to restore their functional behavior *in vivo* [1] and to recover repeatable pseudo-elastic mechanical behaviors [56, 57]. Coincidentally, the equibiaxial force-controlled preconditioning protocol employed here only marginally restored the minimum principal pre-strains of the leaflet (E_A = 0-5%), but drastically exceeded the maximum principal pre-strains (E_A = 42-75%).

An alternative preconditioning protocol is warranted so that this refinement of the preconditioning protocol could better restore the pre-strained leaflet configuration for more representative biaxial mechanical characterizations. A previous study used the well-established quasi-linear viscoelastic theory to demonstrate that the preconditioning loading *type* is crucial to capture repeatable mechanical behaviors [56]. It is therefore possible that applied equibiaxial tensions are not appropriate for the preconditioning of heart valve leaflets, and other loading ratios better emulating the *in vivo* strains should be considered [15, 16]. Additionally, conducting more rigorous evaluations of the preconditioning protocols [56, 57] or allowing relaxation periods between cycles [58] may further help overcome current preconditioning challenges.

The qualitative analysis of all our results revealed that the tricuspid valve leaflet pre-strains were heterogeneous within the fiducial markers. The leaflets often experienced a combination of compressive and tensile strains compared to the *ex vivo* configuration, with the exception of the post-preconditioned configuration, which consisted mainly of large tensile strains. This is consistent with previous studies that found heterogeneous leaflet behaviors from refined strain fields [59], varying specimen locations [11] or *in vivo* analyses [16]. However, quantitative analysis showed that the regional differences presented here were not statistically significant.

4.1.2. The Impact of Reference Configuration on the Leaflet Biaxial Mechanical Properties

Our use of the reference configurations to determine important biomechanics metrics led us to two key observations. First, the PPC configuration significantly reduced the radial stretch and decreased the mechanical anisotropy (i.e., $AI \approx 1.0$) for the anterior and posterior leaflets. This is somewhat to be expected since we also observed large tensile strains for the PPC configuration with respect to the *ex vivo* configuration. However, it is intriguing that the circumferential direction along with most collagen fibers are aligned [10, 13, 14] did not undergo significant changes in the biomechanically based metrics examined. Second, the septal leaflet contained a unique combination of changes to the biomechanically based metrics that did not significantly alter mechanical anisotropy. Previous studies [10, 14] have also identified distinct microstructural features properties for the septal leaflet, suggesting that the pre-strains may be related to some unique microstructural feature of the tissue. This is discussed in more detail below.

4.1.3. Potential Microstructural Drivers of Leaflet Pre-Strains

The leaflet-specific findings found here can be linked to the underlying microstructure of the leaflet. Previous imaging studies have shown that the collagen fibers of the tricuspid valve leaflet are preferentially aligned near the circumferential direction, with less aligned collagen fiber architectures for the septal leaflet [10, 14]. The large compressive strains we found for the anterior and posterior leaflets after valve explantation were roughly aligned with the circumferential direction. On the other hand, compressive strains for the septal leaflet were less consistently aligned with the circumferential or radial directions. These findings indicate the role of collagen fibers in leaflet pre-strains, consistent with collagen fibers being deposited with a pre-stretch during the growth and remodeling process [60, 61]. Furthermore, our results showed that the radial leaflet stretches calculated with respect to the PPC configuration were significantly smaller than with respect to the other configurations. Since the radial direction is orthogonal to the preferred direction of the collagen fibers, this may have the implications that the collagen fibers may help inhibit unwanted post-preconditioning strains. Further studies, as suggested in Section 4.4, can further explore this key linking between tissue microstructure and observed leaflet pre-strains.

4.2. Comparisons with Existing Literature

To the best of our knowledge, no studies have focused on the pre-strains of the *tricuspid valve leaflet*. Therefore, this subsection focuses on putting our findings in the context of the mitral valve, the aortic valve, and other porcine tissues.

4.2.1. Experimental Characterizations of the Mitral and Aortic Heart Valves

Amini *et al.* [31] were the first to quantify the pre-strains of the mitral valve anterior leaflet *in vivo* using a 2×2 grid of sonocrystals sutured to the central 10×10 mm region of the leaflet. They showed that the leaflet exhibited 16% circumferential pre-strain and 26% radial pre-strain between the 'explanted' and the *in vivo* configuration. The later investigation by Lee *et al.* [32] used five sonocrystals in the central region of $n = 6$ anterior mitral valve leaflets and found average circumferential and radial pre-strains of 32% and 35% between the *in vivo* and '*ex vivo*' configurations. On the other hand, Aggarwal *et al.* [35] showed that the aortic valve cusps shrank by $\sim$ 17% when excised from the heart. Our principal pre-strains (7-21%) are generally smaller than the findings of the mitral valve studies, but in a similar range to the aortic valve study. The discrepancies may be attributed to the differences between the heart valves [9, 62–64], or they could be due to our lack of the *in vivo* unloaded tricuspid valve configuration compared to those sonocrystal-based studies. The data of Amini *et al.* [31] showed an additional 11% circumferential strain and 1% radial strain between '*ex vivo*' and *in vivo* configurations that can serve to bring our pre-strains to a similar level as the mitral valve

leaflet counterpart. Future *in-silico* investigations could use the 3D finite element models for the TV constructed from segmented medical image data to understand whether our presented pre-strains can provide reasonable predictions of the TV behavior. Discrepancies between segmented TV geometry and *in-silico* predictions allow us to bridge this gap while avoiding the challenges and costs associated with using large animal models.

4.2.2. Computational Investigations of the Mitral Valve

Rausch *et al*. [43] incorporated different pre-strain levels into their finite element model of a simplified mitral valve geometry. They then used this model to fit the experimental sonocrystal deformations using inverse finite element analysis. Their finite element model with 30% homogeneous areal pre-strain provided the best predictions of the uniaxial data presented by May-Newman and Yin [65]. This predicted pre-strain is much larger than our current findings for the tricuspid valve leaflets and the pre-strains presented by Amini *et al*. [31], but agrees better with the more isotropic pre-strains reported by Lee *et al*. [32]. More recently, Prot and Skallerud [66] performed a similar computational investigation using a complete mitral valve apparatus derived from echocardiographic measurements. They found that an areal pre-strain of 22% could result in unrealistic leaflet motions and incomplete leaflet coaptation. Our experimentally determined tricuspid valve leaflet pre-strains fall within this threshold, with the exception for the septal leaflet. Interestingly, this threshold is larger than the experimental findings of Amini *et al*. [31] and Lee *et al*. [32], suggesting that the pre-strains are spatially varying to allow complete closure of the mitral valve. Finally, the study by van Keele *et al*. [44] combined the mitral valve computational model developed by Rausch *et al*. [43] with the mechanobiology model of Loerakker *et al*. [67, 68] to understand if the pre-stretches are related to traction forces generated by cells within the tissue. They found that the cells produced circumferential and radial pre-strains of 18% and 22%, respectively, which were also much larger than the pre-strains presented herein for the tricuspid valve leaflets.

4.2.3. Experimental Characterizations of the Pre-Strains for other Porcine Tissues

Buganza Tepole *et al*. [36] used stereo cameras to determine that the pre-strains of porcine skin were on the order of 23%. The authors later refined their approach to include smaller regions for their pre-strain analysis [37] and discovered substantial variations in the pre-strain that were, on average, much larger than their previous findings. For ventricular tissue, Genet *et al*. [29] used a computational model of the left ventricular wall to understand what degrees of pre-strain generated by growth and remodeling processes could replicate their opening angle experiment. They found that a range of pre-strains (6-17%) resulted in reasonable predictions of the ventricular opening angle. Finally, Sigaeva *et al*. [26] recently expanded the seminal work of Chuong and Fung [1] and found strains ranging from -7% to $+15\%$ throughout the wall of a porcine aorta after incision. Compared to these collective results, it appears that the porcine tricuspid valve leaflet pre-strains are smaller than the skin pre-strains, in a similar range as the left ventricle pre-strains, and possibly larger than the aortic pre-strains. Differences between methodologies and techniques may skew these results, and further studies could compare pre-strains in a more controlled/comparable setting.

4.3. Study Limitations

This study is not without limitations. At first we only focused on the pre-strains within the central 10×10 mm of each leaflet. Previous studies have highlighted the spatially varying properties of the tricuspid valve leaflets [11]. It is also known that the tricuspid valve leaflet layers exhibit unique microstructures and mechanical behaviors [12]. Future studies need to account for these regional and transmural variations when examining the pre-strains or integrating them into computational models of the tricuspid valve. It is also important to explore the potential influence of the tine insertions

on the computed TV leaflet pre-strains. A previous study [69] demonstrated that the proximity of the mounting insertions to the fiducial markers can alter the homogeneity of the strain field and subsequent analyses. Second, user bias in the fiducial marker selection affects the 3D marker locations determined using photogrammetry. We attempted to limit the effects of such bias by having one user for all $n = 8$ porcine hearts. Our verification of the photogrammetry method presented in Appendix A showed small deviations (< 0.5 mm) when comparing the predictions against the ground truth. This user bias may be circumvented via automatic marker selection techniques (e.g., Otsu's method [70]), and the distance errors could potentially be further reduced by expanding the number of cameras used with the direct linear transformation (see Fig. 4 of [36]).

Third, we could only experimentally characterize the *ex vivo* pre-strains of the tricuspid valve leaflets. There are pre-strains released by removing the heart from the animal subject [31] and the pre-strains are likely to be released by opening the right ventricle prior to the placement of the fiducial marker. Future studies should use more controlled animal models in combination with our *ex vivo* techniques to holistically assess the pre-strains of the tricuspid valve leaflets. Finally, our approach did not allow us to monitor changes in the leaflet thickness across the configurations considered herein. It is common for studies focusing on heart valves to assume that the leaflets are incompressible [52, 53], which should be carefully examined in future studies using our pre-strain quantification process.

4.4. Future Extensions

There are several potential extensions to this work in addition to addressing our study limitations (Section 4.3). First, we considered the pre-strains associated with the release of the tissue from its *in situ* environment, but not the intrinsic pre-strains at a specific location. Future investigations may be inspired by a recent tympanic membrane study by Livens *et al*. [39], which used micro-incisions to release the local tissue pre-strains, or by the work of Buganza Tepole *et al*. [37] who sub-divided their porcine skin specimens to reveal local pre-strains. Second, there is substantial evidence from our results that the pre-strains are related to the underlying tissue microstructure. This relationship could be investigated in future works by combining our novel benchtop method with advanced imaging techniques, such as polarized spatial frequency domain imaging (i.e., for collagen fiber architecture) [14], optical coherence tomography (i.e., for microstructural morphology) [71] or multi-photon microscopy (i.e., for constituent distributions) [10]. Finally, we have shown that equibiaxial force-controlled preconditioning to 40 N/m (280 mN) does not appropriately restore the *ex vivo* pre-strains. An extension of this work could determine better *in vitro* techniques to reach tissue pre-strains prior to biaxial mechanical characterizations. These could be different biaxial force ratios, force-controlled vs. displacement-controlled preconditioning, and/or a new protocol that applies strains that match our pre-strains presented in this study. Among other things, these extensions will significantly advance the field of tricuspid valve tissue biomechanics, allowing accurate pre-strains to be accounted for in computational predictions of valve function.

5. Conclusion

This study provided the first benchtop characterization of the tricuspid valve leaflet *ex vivo* pre-strains. We have shown that the tricuspid valve leaflets shrink after excision from the *ex vivo* heart, with the septal leaflet having more compressive changes. These deformations show slight, non-significant spatial variations within the 10×10 mm central leaflet region. Interestingly, no significant differences have been found between the strains in the explanted or dissected configurations for a given leaflet. This further suggests that most of the pre-strains were released from their *in situ* environment by dissecting the valve. The dissected specimens were then mounted on a biaxial testing device to understand how the common stress-free configurations for mechanical characterizations compare to the

ex vivo reference configuration. After attachment to the system, the leaflets were subjected to slight tensile strains from their dissected configuration, but were still compressed from their *ex vivo* configuration. The tensile changes were magnified after equibiaxial preconditioning with significant changes in the maximum principal strain and areal strain. These observed changes in the four configurations were then placed in the context of general biomechanical metrics obtained during biaxial mechanical testing. An important observation from this analysis was that the large tensile strains applied on the tissue after preconditioning resulted in significant underestimates of radial tissue stretches and material anisotropy. This observation leads us to believe that the equibiaxial force-controlled preconditioning protocol used is not ideal for restoring the *in vivo* behavior of the tricuspid valve leaflets. Extensions of this work should determine a more appropriate tricuspid valve-specific preconditioning protocol.

Appendix A. Three-Dimensional Photogrammetry using Direct Linear Transformation

In this appendix, we describe the direct linear transformation used for three-dimensional photogrammetry in this study. We also detail the calibration of our stereo camera setup used in Section 2.2.

Direct Linear Transformation Considering a point O in 3D space, a direct linear transformation [49, 72] can be used to transform its 3D location (x, y, z) to the pixel coordinates of a camera (p, q) via

$$p = \frac{Ax + By + Cz + D}{Ix + Jy + Kz + 1}, \quad q = \frac{Ex + Fy + Gz + H}{Ix + Jy + Kz + 1}, \tag{A.1}$$

where $\{A, B, C, \ldots, I, J, K\}$ are the camera-specific coefficients that depend on the camera's properties (e.g., focal length) and the overall configuration. At least six non-coplanar points with known (x_i, y_i, z_i) are required to determine the 11 unknown coefficients $\{A, B, C, \ldots, I, J, K\}$ by solving the following overdetermined linear system of equations, i.e.,

$$\begin{bmatrix} x_1 & y_1 & z_1 & 1 & 0 & 0 & 0 & 0 & -p_1x_1 & -p_1y_1 & -p_1z_1 \\ 0 & 0 & 0 & 0 & x_1 & y_1 & z_1 & 1 & -q_1x_1 & -q_1y_1 & -q_1z_1 \\ \vdots & \vdots & \vdots & \vdots & \vdots & \vdots & \vdots & \vdots & \vdots & \vdots & \vdots \\ x_n & y_n & z_n & 1 & 0 & 0 & 0 & 0 & -p_nx_n & -p_ny_n & -p_nz_n \\ 0 & 0 & 0 & 0 & x_n & y_n & z_n & 1 & -q_nx_n & -q_ny_n & -q_nz_n \end{bmatrix} \begin{Bmatrix} A \\ B \\ \vdots \\ J \\ K \end{Bmatrix} = \begin{Bmatrix} p_1 \\ q_1 \\ \vdots \\ p_n \\ q_n \end{Bmatrix}. \tag{A.2}$$

The above calibration procedure is repeated for two cameras with non-planar views to obtain the coefficient sets $\{A^{[1]}, B^{[1]}, C^{[1]}, \ldots, I^{[1]}, J^{[1]}, K^{[1]}\}$ and $\{A^{[2]}, B^{[2]}, C^{[2]}, \ldots, I^{[2]}, J^{[2]}, K^{[2]}\}$.

Once these camera-specific unknown coefficients are calibrated, the pixel coordinates from the two cameras $(p_I^{[1]}, q_I^{[1]})$ and $(p_I^{[2]}, q_I^{[2]})$ for each fiducial marker can then be used to determine the fiducial marker location in the 3D space (x_I, y_I, z_I) by solving the linear equations

$$\begin{bmatrix} \left(A^{[1]} - p_I^{[1]} I^{[1]}\right) & \left(B^{[1]} - p_I^{[1]} J^{[1]}\right) & \left(C^{[1]} - p_I^{[1]} K^{[1]}\right) \\ \left(E^{[1]} - q_I^{[1]} I^{[1]}\right) & \left(F^{[1]} - q_I^{[1]} J^{[1]}\right) & \left(G^{[1]} - q_I^{[1]} K^{[1]}\right) \\ \left(A^{[2]} - p_I^{[2]} I^{[2]}\right) & \left(B^{[2]} - p_I^{[2]} J^{[2]}\right) & \left(C^{[2]} - p_I^{[2]} K^{[2]}\right) \\ \left(E^{[2]} - q_I^{[2]} I^{[2]}\right) & \left(F^{[2]} - q_I^{[2]} J^{[2]}\right) & \left(G^{[2]} - q_I^{[2]} K^{[2]}\right) \end{bmatrix} \begin{Bmatrix} x_I \\ y_I \\ z_I \end{Bmatrix} = \begin{Bmatrix} \left(D^{[1]} - p_I^{[1]}\right) \\ \left(H^{[1]} - q_I^{[1]}\right) \\ \left(D^{[2]} - p_I^{[2]}\right) \\ \left(H^{[2]} - q_I^{[2]}\right) \end{Bmatrix}. \tag{A.3}$$

Stereo Camera Calibration We calibrated the direct linear transformations for our two cameras using a 3D-printed half-cylinder covered with gridded calibration markers (Fig. A1). The cylinder was placed approximately 20 cm away from each camera. A calibration image was taken from each camera

and imported into MATLAB (MathWorks, Natick, MA) where we used the `drawpolygon()` function to determine the pixel locations of the 42 visible calibration points.

The system of equations in Eq. (A.2) requires at least six non-coplanar calibration points to determine the camera-specific coefficients $\{A, B, C, \ldots, I, J, K\}$ for each camera. However, it is not known how the number of calibration points (≥ 6) or their arrangement would affect the resulting 3D photogrammtery results. Therefore, we further investigated these important considerations through the 5 calibration scenarios as depicted in Fig. A2 and Table A1. For each scenario, the camera-specific coefficients were determined using a subset of the calibration markers (denoted by the box in Fig. A2), which were then used to predict the 3D locations of all other calibration markers.

The predicted 3D marker locations were compared with the known marker locations (determined from the given half-cylindrical geometry) to calculate the average distance errors (Table A1). It is clear that more than six calibration markers are needed to avoid large errors in the predicted marker locations (Fig. A2(a)). However, the error can be quickly minimized by increasing the number of calibrated points (Fig. A2(b)-(d)) or by ensuring that the 3D photogrammetry predictions fall within the calibration markers (Fig. A2(e)). We were satisfied with the minimum error for our 3D photogrammetry (0.24 mm) considering the tricuspid valve tissue is typically in or near the calibrated region. However, further investigations are warranted to explore the extrapolative capabilities of this photogrammetry method and calibration process.

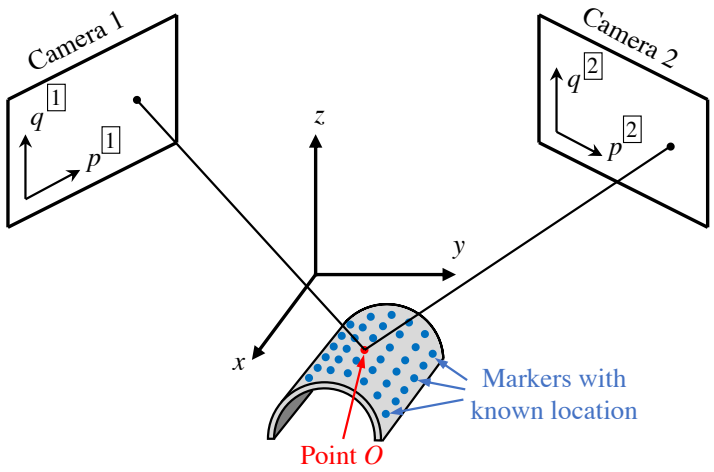

Figure A1: Schematic of the calibration of the direct linear transformation with two cameras via a gridded cylinder.

Table A1: Computed average distance errors of the direct linear transformation calibration scenarios (see also Fig. A2).

Scenario	Number of Calibration Markers	Marker Location	Avg. Error (mm) Calibrated	Avg. Error (mm) Non-Calibrated
1	6	Along Border Center	1.04 mm 1.44 mm	1.77 mm 3.00 mm
2	14	Along Border Center	0.46 mm 0.41 mm	0.63 mm 0.49 mm
3	28	Along Border Center	0.24 mm 0.25 mm	0.25 mm 0.30 mm
4	42	All Markers	0.24 mm	N/A
5	22	Boundary Markers	0.26 mm	0.23 mm

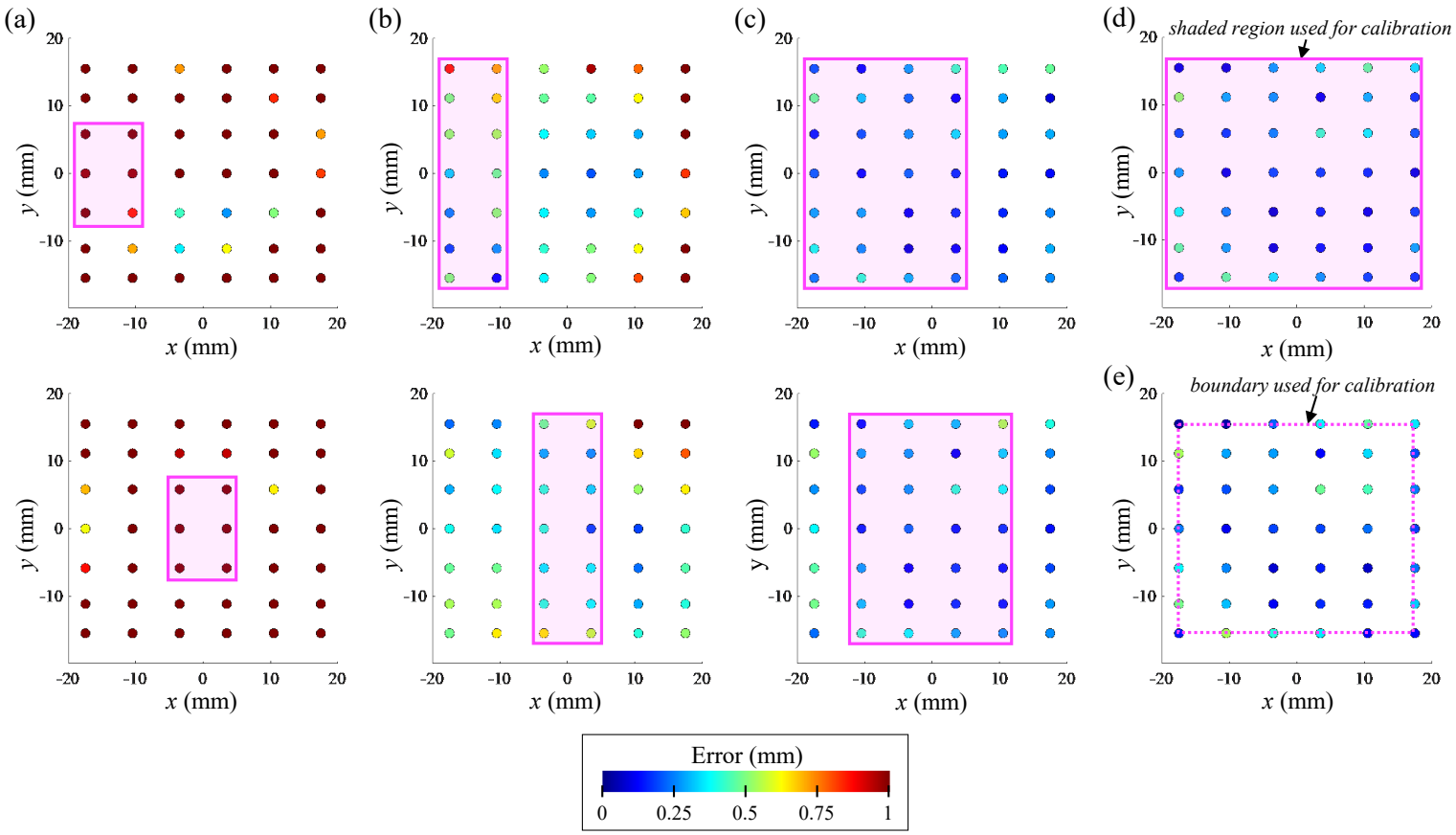

Figure A2: Calculated distance error of 42 marks on the calibration cylinder surface using a subset of the marks for camera-specific coefficient calibration: (a) the 6 marks (*top*) along the boundary, and (*bottom*) in the center, (b) the 14 marks (*top*) along the boundary and (*bottom*) in the center, (c) the 28 marks (*top*) along the boundary and (*bottom*) in the center, (d) all 42 marks, and (e) the 22 marks along the perimeter.

Appendix B. Reproducing Kernel Method for Computing Leaflet Strains

In this appendix we describe the reproducing kernel (RK) meshfree method [47, 48], with which we calculated the shape function derivatives in the calculation of the deformation gradient $\mathbf{F}$ (see Section 2.4) and the isoparametric generation of material points (i.e., visualization grid points) based on the 9 fiducial markers.

Reproducing Kernel Method The RK shape function of the I^{th} material point $[\mathbf{x}_I] = [x_I, y_I, z_I]^{\mathrm{T}}$ has the form

$$\Psi_I(\mathbf{x}) = \mathbf{H}^{\mathrm{T}}(\mathbf{0})\mathbf{M}^{-1}(\mathbf{x})\mathbf{H}(\mathbf{x}-\mathbf{x}_I)\Phi(\mathbf{x}-\mathbf{x}_I;\mathbf{a}), \tag{A.4}$$

where $[\mathbf{H}(\mathbf{x})] = [1, x, y, z]^{\mathrm{T}}$ contains the basis function vector of monomials (up to the first order chosen for the present study), $\Phi(\mathbf{x}-\mathbf{x}_I;\mathbf{a})$ is the kernel function with support radii $[\mathbf{a}] = [a_x, a_y, a_z]^{\mathrm{T}}$, and $\mathbf{M}(\mathbf{x})$ is the moment matrix defined as

$$\mathbf{M}(\mathbf{x}) = \sum_{I=1}^{NP} \mathbf{H}(\mathbf{x}-\mathbf{x}_I)\mathbf{H}^{\mathrm{T}}(\mathbf{x}-\mathbf{x}_I)\Phi(\mathbf{x}-\mathbf{x}_I;\mathbf{a}). \tag{A.5}$$

For the purpose of this study, $\Phi(\mathbf{x}-\mathbf{x}_I;\mathbf{a})$ is chosen as the product of one-dimensional kernel functions, i.e.,

$$\Phi(\mathbf{x}-\mathbf{x}_I;\mathbf{a}) = \frac{1}{a_x a_y a_z}\bar{\Phi}\left(\left|\frac{x-x_I}{a_x}\right|\right)\bar{\Phi}\left(\left|\frac{y-y_I}{a_y}\right|\right)\bar{\Phi}\left(\left|\frac{z-z_I}{a_z}\right|\right), \tag{A.6}$$

where the one-dimensional kernel functions for all three spatial coordinates x, y, and z take the form of a cubic B-spline function, i.e.,

$$\bar{\Phi}(t) = \begin{cases} \frac{2}{3} - 4t^2 + 4t^3, & \text{for } 0 \le t \le \frac{1}{2}, \\ \frac{4}{3} - 4t + 4t^2 - \frac{4}{3}t^3, & \text{for } \frac{1}{2} \le t \le 1, \\ 0, & \text{otherwise.} \end{cases} \tag{A.7}$$

The partial derivatives of the shape function $\Psi_I(\mathbf{x})$ with respect to the three spatial coordinates were then determined using

$$\begin{aligned} \nabla_{\mathbf{x}}\Psi_I(\mathbf{x}) = \mathbf{H}^{\mathrm{T}}(\mathbf{0})[&\nabla_{\mathbf{x}}\mathbf{M}^{-1}(\mathbf{x})\mathbf{H}(\mathbf{x}-\mathbf{x}_I)\Phi(\mathbf{x}-\mathbf{x}_I;\mathbf{a}) + \mathbf{M}^{-1}(\mathbf{x})\nabla_{\mathbf{x}}\mathbf{H}(\mathbf{x}-\mathbf{x}_I)\Phi(\mathbf{x}-\mathbf{x}_I;\mathbf{a}) \\ &+ \mathbf{M}^{-1}(\mathbf{x})\mathbf{H}(\mathbf{x}-\mathbf{x}_I)\nabla_{\mathbf{x}}(\mathbf{x}-\mathbf{x}_I;\mathbf{a})]. \end{aligned} \tag{A.8}$$

In this relationship, $\nabla_{\mathbf{x}}(\bullet)$ denotes the gradient operator with respect to the spatial coordinates (x, y, z), $\nabla_{\mathbf{x}}\mathbf{M}^{-1}(\mathbf{x}) = -\mathbf{M}^{-1}(\mathbf{x})\nabla_{\mathbf{x}}\mathbf{M}(\mathbf{x})\mathbf{M}^{-1}(\mathbf{x})$, and $\nabla_{\mathbf{x}}\mathbf{M}(\mathbf{x})$ can be algebraically derived from Eq. (A.5).

Isoparametric Generation of Material Points The 3×3 fiducial marker array (Fig. 2(b)) was considered as a 9-node finite element in the parametric domain (ξ, η), which is defined with the following shape functions

$$\begin{aligned} &N_1(\xi,\eta) = \frac{1}{4}(\xi^2-\xi)(\eta^2-\eta), \quad N_2(\xi,\eta) = \frac{1}{4}(\xi^2+\xi)(\eta^2-\eta), \quad N_3(\xi,\eta) = \frac{1}{4}(\xi^2+\xi)(\eta^2+\eta), \\ &N_4(\xi,\eta) = \frac{1}{4}(\xi^2-\xi)(\eta^2+\eta), \quad N_5(\xi,\eta) = \frac{1}{2}(1-\xi^2)(\eta^2-\eta), \quad N_6(\xi,\eta) = \frac{1}{2}(\xi^2+\xi)(1-\eta^2), \\ &N_7(\xi,\eta) = \frac{1}{2}(1-\xi^2)(\eta^2+\eta), \quad N_8(\xi,\eta) = \frac{1}{2}(\xi^2-\xi)(1-\eta^2), \quad N_9(\xi,\eta) = (1-\xi^2)(1-\eta^2). \end{aligned} \tag{A.9}$$

The shape functions of the single 9-node finite element were combined with the (x, y, z) coordinates of the nine fiducial markers to generate a 25×25 visualization grid of *material points*. These visualization grid points were used for the subsequent computations of the deformation gradient $\mathbf{F}$ in Section 2.4.

Declaration of Competing Interest. The authors declare that they have no known competing financial interests or personal relationships that could have appeared to influence (bias) the work reported in this manuscript.

Acknowledgments. Supports from the American Heart Association (AHA) Scientist Development Grant Award (16SDG27760143) and the Presbyterian Health Foundation Team Science Grant are greatly appreciated. CHL was in part supported by research funding from the OU Research Council. DWL and CJR were supported by the National Science Foundation Graduate Research Fellowship (GRF 2019254233 and 2020307284). DWL was supported in part by the AHA Predoctoral Fellowship (Grant No. 821298).

References

[1] C.-J. Chuong, Y.-C. Fung, Residual Stress in Arteries, in: Frontiers in Biomechanics, Springer, 1986, pp. 117–129. doi:10.1007/978-1-4612-4866-8_9.

[2] G. D. Dreyfus, P. J. Corbi, K. J. Chan, T. Bahrami, Secondary tricuspid regurgitation or dilatation: Which should be the criteria for surgical repair?, The Annals of Thoracic Surgery 79 (1) (2005) 127–132. doi:10.1016/j.athoracsur.2004.06.057.

[3] A. C. Anyanwu, D. H. Adams, Functional tricuspid regurgitation in mitral valve disease: Epidemiology and prognostic implications, in: Seminars in Thoracic and Cardiovascular Surgery, Vol. 22, Elsevier, 2010, pp. 69–75. doi:10.1053/j.semtcvs.2010.05.006.

[4] W. D. Meador, M. Mathur, M. K. Rausch, Tricuspid Valve Biomechanics: A Brief Review, in: Advances in Heart Valve Biomechanics, Springer, 2018, pp. 105–114. doi:10.1007/978-3-030-01993-8_5.

[5] C.-H. Lee, D. W. Laurence, C. J. Ross, K. E. Kramer, A. R. Babu, E. L. Johnson, M.-C. Hsu, A. Aggarwal, A. Mir, H. M. Burkhart, R. A. Towner, R. Baumwart, Y. Wu, Mechanics of the tricuspid valve—From clinical diagnosis/treatment, in-vivo and in-vitro investigations, to patient-specific biomechanical modeling, Bioengineering 6 (2) (2019) 47. doi:10.3390/bioengineering6020047.

[6] K. May-Newman, F. Yin, Biaxial mechanical behavior of excised porcine mitral valve leaflets, American Journal of Physiology-Heart and Circulatory Physiology 269 (4) (1995) H1319–H1327. doi:10.1152/ajpheart.1995.269.4.H1319.

[7] M. S. Sacks, Biaxial mechanical evaluation of planar biological materials, Journal of Elasticity and the Physical Science of Solids 61 (1) (2000) 199–246. doi:10.1023/A:1010917028671.

[8] K. Amini Khoiy, R. Amini, On the biaxial mechanical response of porcine tricuspid valve leaflets, Journal of Biomechanical Engineering 138 (10) (2016) 104504. doi:10.1115/1.4034426.

[9] S. V. Jett, D. W. Laurence, R. K. Kunkel, A. R. Babu, K. E. Kramer, R. Baumwart, R. A. Towner, Y. Wu, C.-H. Lee, An investigation of the anisotropic mechanical properties and anatomical structure of porcine atrioventricular heart valves, Journal of the Mechanical Behavior of Biomedical Materials 87 (2018) 155–171. doi:10.1016/j.jmbbm.2018.07.024.

[10] W. D. Meador, M. Mathur, G. P. Sugerman, T. Jazwiec, M. Malinowski, M. R. Bersi, T. A. Timek, M. K. Rausch, A detailed mechanical and microstructural analysis of ovine tricuspid valve leaflets, Acta Biomaterialia 102 (2020) 100–113. doi:10.1016/j.actbio.2019.11.039.

[11] D. W. Laurence, C. J. Ross, S. V. Jett, C. H. Johns, A. Echols, R. Baumwart, R. Towner, J. Liao, P. Bajona, Y. Wu, C.-H. Lee, An investigation of regional variations in the biaxial mechanical properties and stress relaxation behaviors of porcine atrioventricular heart valve leaflets, Journal of Biomechanics 83 (2019) 16–27. doi:10.1016/j.jbiomech.2018.11.015.

[12] K. E. Kramer, C. J. Ross, D. W. Laurence, A. R. Babu, Y. Wu, R. A. Towner, A. Mir, H. M. Burkhart, G. A. Holzapfel, C.-H. Lee, An investigation of layer-specific tissue biomechanics of porcine atrioventricular valve anterior leaflets, Acta Biomaterialia 96 (2019) 368–384. doi:10.1016/j.actbio.2019.06.049.

[13] V. S. Thomas, V. Lai, R. Amini, A computational multi-scale approach to investigate mechanically-induced changes in tricuspid valve anterior leaflet microstructure, Acta Biomaterialia 94 (2019) 524–535. doi:10.1016/j.actbio.2019.05.074.

[14] L. T. Hudson, S. V. Jett, K. E. Kramer, D. W. Laurence, C. J. Ross, R. A. Towner, R. Baumwart, K. M. Lim, A. Mir, H. M. Burkhart, et al., A pilot study on linking tissue mechanics with load-dependent collagen microstructures in porcine tricuspid valve leaflets, Bioengineering 7 (2) (2020) 60. doi:10.3390/bioengineering7020060.

[15] K. Amini Khoiy, D. Biswas, T. N. Decker, K. T. Asgarian, F. Loth, R. Amini, Surface strains of porcine tricuspid valve septal leaflets measured in *ex vivo* beating hearts, Journal of Biomechanical Engineering 138 (11) (2016) 111006. doi:10.1115/1.4034621.

[16] M. Mathur, T. Jazwiec, W. Meador, M. Malinowski, M. Goehler, H. Ferguson, T. Timek, M. Rausch, Tricuspid valve leaflet strains in the beating ovine heart, Biomechanics and Modeling in Mechanobiology 18 (5) (2019) 1351–1361. doi:10.1007/s10237-019-01148-y.

[17] F. Kong, T. Pham, C. Martin, R. McKay, C. Primiano, S. Hashim, S. Kodali, W. Sun, Finite element analysis of tricuspid valve deformation from multi-slice computed tomography images, Annals of Biomedical Engineering 46 (8) (2018) 1112–1127. doi:10.1007/s10439-018-2024-8.

[18] S. Singh-Gryzbon, V. Sadri, M. Toma, E. L. Pierce, Z. A. Wei, A. P. Yoganathan, Development of a computational method for simulating tricuspid valve dynamics, Annals of Biomedical Engineering 47 (6) (2019) 1422–1434. doi:10.1007/s10439-019-02243-y.

[19] M. Stevanella, E. Votta, M. Lemma, C. Antona, A. Redaelli, Finite element modelling of the tricuspid valve: A preliminary study, Medical Engineering and Physics 32 (10) (2010) 1213–1223. doi:10.1016/j.medengphy.2010.08.013.

[20] E. L. Johnson, D. W. Laurence, F. Xu, C. E. Crisp, A. Mir, H. M. Burkhart, C.-H. Lee, M.-C. Hsu, Parameterization, geometric modeling, and isogeometric analysis of tricuspid valves, Computer Methods in Applied Mechanics and Engineering 384 (2021) 113960.

[21] D. W. Laurence, E. L. Johnson, M.-C. Hsu, R. Baumwart, A. Mir, H. M. Burkhart, G. A. Holzapfel, Y. Wu, C.-H. Lee,

A pilot *in silico* modeling-based study of the pathological effects on the biomechanical function of tricuspid valves, International Journal for Numerical Methods in Biomedical Engineering 36 (7) (2020) e3346. doi:10.1002/cnm.3346.

[22] C.-H. Lee, R. Amini, R. C. Gorman, J. H. Gorman III, M. S. Sacks, An inverse modeling approach for stress estimation in mitral valve anterior leaflet valvuloplasty for in-vivo valvular biomaterial assessment, Journal of Biomechanics 47 (9) (2014) 2055–2063. doi:10.1016/j.jbiomech.2013.10.058.

[23] J. H. Omens, Y.-C. Fung, Residual strain in rat left ventricle., Circulation research 66 (1) (1990) 37–45.

[24] Y. Fung, S. Liu, Change of residual strains in arteries due to hypertrophy caused by aortic constriction., Circulation research 65 (5) (1989) 1340–1349.

[25] G. Dusfour, D. Ambard, P. Cañadas, S. Lefloch, Residual strains estimation in the annulus fibrosus through digital image correlation, Journal of Theoretical, Computational and Applied Mechanics (2021) 1–15doi:10.46298/jtcam.6971.

[26] T. Sigaeva, M. Destrade, E. S. Di Martino, Multi-sector approximation method for arteries: The residual stresses of circumferential rings with non-trivial openings, Journal of the Royal Society Interface 16 (156) (2019) 20190023. doi:10.1098/rsif.2019.0023.

[27] T. Sigaeva, G. Sommer, G. A. Holzapfel, E. S. Di Martino, Anisotropic residual stresses in arteries, Journal of the Royal Society Interface 16 (151) (2019) 20190029. doi:10.1098/rsif.2019.0029.

[28] A. Utrera, Á. Navarrete, A. González-Candia, C. García-Herrera, E. A. Herrera, Biomechanical and structural responses of the aorta to intermittent hypobaric hypoxia in a rat model, Scientific Reports 12 (2022) 3790. doi:10.1038/s41598-022-07616-3.

[29] M. Genet, M. Rausch, L. C. Lee, S. Choy, X. Zhao, G. S. Kassab, S. Kozerke, J. M. Guccione, E. Kuhl, Heterogeneous growth-induced prestrain in the heart, Journal of Biomechanics 48 (10) (2015) 2080–2089. doi:10.1016/j.jbiomech.2015.03.012.

[30] X. Shi, Y. Liu, K. M. Copeland, S. R. McMahan, S. Zhang, J. R. Butler, Y. Hong, M. Cho, P. Bajona, H. Gao, J. Liao, Epicardial prestrained confinement and residual stresses: A newly observed heart ventricle confinement interface, Journal of the Royal Society Interface 16 (152) (2019) 20190028. doi:10.1098/rsif.2019.0028.

[31] R. Amini, C. E. Eckert, K. Koomalsingh, J. McGarvey, M. Minakawa, J. H. Gorman, R. C. Gorman, M. S. Sacks, On the *in vivo* deformation of the mitral valve anterior leaflet: Effects of annular geometry and referential configuration, Annals of Biomedical Engineering 40 (7) (2012) 1455–1467. doi:10.1007/s10439-012-0524-5.

[32] C.-H. Lee, W. Zhang, K. Feaver, R. C. Gorman, J. H. Gorman, M. S. Sacks, On the *in vivo* function of the mitral heart valve leaflet: insights into tissue–interstitial cell biomechanical coupling, Biomechanics and Modeling in Mechanobiology 16 (5) (2017) 1613–1632. doi:10.1007/s10237-017-0908-4.

[33] I. Vesely, R. Noseworthy, Micromechanics of the fibrosa and the ventricularis in aortic valve leaflets, Journal of Biomechanics 25 (1) (1992) 101–113. doi:10.1016/0021-9290(92)90249-Z.

[34] I. Vesely, A. Lozon, E. Talman, Is zero-pressure fixation of bioprosthetic valves truly stress free?, The Journal of Thoracic and Cardiovascular Surgery 106 (2) (1993) 288–298. doi:10.1016/S0022-5223(19)34128-5.

[35] A. Aggarwal, A. M. Pouch, E. Lai, J. Lesicko, P. A. Yushkevich, J. H. Gorman III, R. C. Gorman, M. S. Sacks, In-vivo heterogeneous functional and residual strains in human aortic valve leaflets, Journal of Biomechanics 49 (12) (2016) 2481–2490. doi:10.1016/j.jbiomech.2016.04.038.

[36] A. Buganza Tepole, M. Gart, C. A. Purnell, A. K. Gosain, E. Kuhl, Multi-view stereo analysis reveals anisotropy of prestrain, deformation, and growth in living skin, Biomechanics and Modeling in Mechanobiology 14 (5) (2015) 1007–1019. doi:10.1007/s10237-015-0650-8.

[37] A. Buganza Tepole, M. Gart, C. A. Purnell, A. K. Gosain, E. Kuhl, The incompatibility of living systems: Characterizing growth-induced incompatibilities in expanded skin, Annals of Biomedical Engineering 44 (5) (2016) 1734–1752. doi:10.1007/s10439-015-1467-4.

[38] W. D. Meador, G. P. Sugerman, H. M. Story, A. W. Seifert, M. R. Bersi, A. B. Tepole, M. K. Rausch, The regional-dependent biaxial behavior of young and aged mouse skin: A detailed histomechanical characterization, residual strain analysis, and constitutive model, Acta Biomaterialia 101 (2020) 403–413. doi:10.1016/j.actbio.2019.10.020.

[39] P. Livens, P. G. Muyshondt, J. J. Dirckx, Prestrain in the rabbit eardrum measured by digital image correlation and micro-incisions, Hearing Research 412 (2021) 108392. doi:10.1016/j.heares.2021.108392.

[40] A. Hoger, Virtual configurations and constitutive equations for residually stressed bodies with material symmetry, Journal of Elasticity 48 (2) (1997) 125–144.

[41] B. E. Johnson, A. Hoger, The use of a virtual configuration in formulating constitutive equations for residually stressed elastic materials, Journal of Elasticity 41 (3) (1995) 177–215.

[42] M. K. Rausch, E. Kuhl, On the effect of prestrain and residual stress in thin biological membranes, Journal of the Mechanics and Physics of Solids 61 (9) (2013) 1955–1969. doi:10.1016/j.jmps.2013.04.005.

[43] M. K. Rausch, N. Famaey, T. O. Shultz, W. Bothe, D. C. Miller, E. Kuhl, Mechanics of the mitral valve: A critical re-

view, an in vivo parameter identification, and the effect of prestrain, Biomechanics and Modeling in Mechanobiology 12 (5) (2013) 1053–1071. doi:10.1007/s10237-012-0462-z.

[44] M. van Kelle, M. Rausch, E. Kuhl, S. Loerakker, A computational model to predict cell traction-mediated prestretch in the mitral valve, Computer Methods in Biomechanics and Biomedical Engineering 22 (15) (2019) 1174–1185. doi:10.1080/10255842.2019.1647533.

[45] A. Drach, A. H. Khalighi, M. S. Sacks, A comprehensive pipeline for multi-resolution modeling of the mitral valve: Validation, computational efficiency, and predictive capability, International Journal for Numerical Methods in Biomedical Engineering 34 (2) (2018) e2921. doi:10.1002/cnm.2921.

[46] W. Zhang, G. Sommer, J. A. Niestrawska, G. A. Holzapfel, D. Nordsletten, The effects of viscoelasticity on residual strain in aortic soft tissues, Acta Biomaterialia 140 (2022) 398–411. doi:10.1016/j.actbio.2021.11.019.

[47] J.-S. Chen, C. Pan, C.-T. Wu, W. K. Liu, Reproducing kernel particle methods for large deformation analysis of non-linear structures, Computer Methods in Applied Mechanics and Engineering 139 (1-4) (1996) 195–227. doi:10.1016/S0045-7825(96)01083-3.

[48] S.-W. Chi, C.-H. Lee, J.-S. Chen, P.-C. Guan, A level set enhanced natural kernel contact algorithm for impact and penetration modeling, International Journal for Numerical Methods in Engineering 102 (2014) 20–27. doi:https://doi.org/10.1002/nme.4728.

[49] A. K. Iyengar, H. Sugimoto, D. B. Smith, M. S. Sacks, Dynamic *in vitro* quantification of bioprosthetic heart valve leaflet motion using structured light projection, Annals of Biomedical Engineering 29 (11) (2001) 963–973. doi:10.1114/1.1415523.

[50] S. V. Jett, L. T. Hudson, R. Baumwart, B. N. Bohnstedt, A. Mir, H. M. Burkhart, G. A. Holzapfel, Y. Wu, C.-H. Lee, Integration of polarized spatial frequency domain imaging (pSFDI) with a biaxial mechanical testing system for quantification of load-dependent collagen architecture in soft collagenous tissues, Acta Biomaterialia 102 (2020) 149–168.

[51] G. A. Holzapfel, Nonlinear Solid Mechanics. A Continuum Approach for Engineering, John Wiley & Sons, Chichester, 2000.

[52] W. Zhang, S. Ayoub, J. Liao, M. S. Sacks, A meso-scale layer-specific structural constitutive model of the mitral heart valve leaflets, Acta Biomaterialia 32 (2016) 238–255. doi:10.1016/j.actbio.2015.12.001.

[53] B. V. Rego, M. S. Sacks, A functionally graded material model for the transmural stress distribution of the aortic valve leaflet, Journal of Biomechanics 54 (2017) 88–95. doi:10.1016/j.jbiomech.2017.01.039.

[54] J. O. Wobbrock, L. Findlater, D. Gergle, J. J. Higgins, The aligned rank transform for nonparametric factorial analyses using only anova procedures, in: Proceedings of the SIGCHI Conference on Human Factors in Computing Systems, 2011, pp. 143–146. doi:10.1145/1978942.1978963.

[55] L. A. Elkin, M. Kay, J. J. Higgins, J. O. Wobbrock, An aligned rank transform procedure for multifactor contrast tests, in: The 34th Annual ACM Symposium on User Interface Software and Technology, 2021, pp. 754–768. doi:10.1145/3472749.3474784.

[56] E. Carew, J. Barber, I. Vesely, Role of preconditioning and recovery time in repeated testing of aortic valve tissues: validation through quasilinear viscoelastic theory, Annals of Biomedical Engineering 28 (9) (2000) 1093–1100.

[57] E. O. Carew, A. Garg, J. E. Barber, I. Vesely, Stress relaxation preconditioning of porcine aortic valves, Annals of Biomedical Engineering 32 (4) (2004) 563–572.

[58] G. Bianco, A. M. Levy, R. Grytz, M. A. Fazio, Effect of different preconditioning protocols on the viscoelastic inflation response of the posterior sclera, Acta Biomaterialia 128 (2021) 332–345.

[59] C. M. Dover, W. Goth, C. Goodbrake, J. W. Tunnell, M. S. Sacks, Simultaneous wide-field planar strain-fiber orientation distribution measurement using polarized spatial domain imaging, Annals of Biomedical Engineering 50 (2022) 253–277. doi:10.1007/s10439-021-02889-7.

[60] Y. Lanir, Mechanistic micro-structural theory of soft tissues growth and remodeling: Tissues with unidirectional fibers, Biomechanics and Modeling in Mechanobiology 14 (2) (2015) 245–266. doi:10.1007/s10237-014-0600-x.

[61] C. Cyron, J. Humphrey, Growth and remodeling of load-bearing biological soft tissues, Meccanica 52 (3) (2017) 645–664. doi:10.1007/s11012-016-0472-5.

[62] K. L. Billiar, M. S. Sacks, Biaxial mechanical properties of the natural and glutaraldehyde treated aortic valve cusp—part I: Experimental results, Journal of Biomechanical Engineering 122 (1) (2000) 23–30. doi:10.1115/1.429624.

[63] L. T. Hudson, D. W. Laurence, H. M. Lau, B. T. Mullins, D. D. Doan, C.-H. Lee, Linking collagen fiber architecture to tissue-level biaxial mechanical behaviors of porcine semilunar heart valve cusps, Journal of the Mechanical Behavior of Biomedical Materials 125 (2022) 104907. doi:10.1016/j.jmbbm.2021.104907.

[64] D. Fitzpatrick, K. Pham, C. J. Ross, L. T. Hudson, L. D. W., Y. Yue, C.-H. Lee, *Ex vivo* experimental characterizations for understanding the interrelationship between tissue mechanics and collagen microstructure of porcine mitral valve leaflets, Journal of the Mechanical Behavior of Biomedical Materials (2022, in press). doi:https://doi.org/10.

1016/j.jmbbm.2022.105401.
[65] K. May-Newman, F. Yin, A constitutive law for mitral valve tissue, Journal of Biomechanical Engineering 120 (1) (1998) 38–47. doi:10.1115/1.2834305.
[66] V. Prot, B. Skallerud, Contributions of prestrains, hyperelasticity, and muscle fiber activation on mitral valve systolic performance, International Journal for Numerical Methods in Biomedical Engineering 33 (4) (2017) e2806. doi:10.1002/cnm.2806.
[67] S. Loerakker, C. Obbink-Huizer, F. Baaijens, A physically motivated constitutive model for cell-mediated compaction and collagen remodeling in soft tissues, Biomechanics and Modeling in Mechanobiology 13 (5) (2014) 985–1001. doi:10.1007/s10237-013-0549-1.
[68] S. Loerakker, T. Ristori, F. P. Baaijens, A computational analysis of cell-mediated compaction and collagen remodeling in tissue-engineered heart valves, Journal of the Mechanical Behavior of Biomedical Materials 58 (2016) 173–187. doi:10.1016/j.jmbbm.2015.10.001.
[69] H. Fehervary, M. Smoljkić, J. Vander Sloten, N. Famaey, Planar biaxial testing of soft biological tissue using rakes: A critical analysis of protocol and fitting process, Journal of the mechanical behavior of biomedical materials 61 (2016) 135–151.
[70] N. Otsu, A threshold selection method from gray-level histograms, IEEE Transactions on Systems, Man, and Cybernetics 9 (1) (1979) 62–66. doi:10.1109/TSMC.1979.4310076.
[71] D. W. Laurence, H. Homburg, F. Yan, Q. Tang, K.-M. Fung, B. N. Bohnstedt, G. A. Holzapfel, C.-H. Lee, A pilot study on biaxial mechanical, collagen microstructural, and morphological characterizations of a resected human intracranial aneurysm tissue, Scientific Reports 11 (2021) 3525. doi:10.1038/s41598-021-82991-x.
[72] N. R. Miller, R. Shapiro, T. M. McLaughlin, A technique for obtaining spatial kinematic parameters of segments of biomechanical systems from cinematographic data, Journal of Biomechanics 13 (7) (1980) 535–547. doi:10.1016/0021-9290(80)90054-8.